Texas A&M University
Mechanical Engineering Department
Turbomachinery Laboratory
Tribology Group

EFFECT OF LUBRICANT SUPPLY PRESSURE ON SFD PERFORMANCE:
ENDS SEALED WITH O-RINGS AND PISTON RINGS

Research Progress Report to the TAMU Turbomachinery Research Consortium

TRC-SFD-01-2017

by

Luis San Andrés
Mast-Childs Chair Professor
Principal Investigator

Bonjin Koo
Research Assistant

Leping Yu
Research Assistant

May 2017

EXECUTIVE SUMMARY
EFFECT OF LUBRICANT SUPPLY PRESSURE ON SFD PERFORMANCE: ENDS SEALED WITH O-RINGS AND PISTON RINGS

LUIS SAN ANDRÉS, BONJIN KOO, AND LEPING YU, MAY 2017

A well-designed SFD must deliver enough damping to aid in decreasing rotor amplitudes of motion. Sealed end SFDs effectively deliver damping in a short length configuration. Piston rings (PRs) and O-rings (ORs) are commonly used as end seals in dampers for commercial and military gas turbine engines, respectively.

Experiments in 2016-2017 produced damping and inertia coefficients for a short length SFD (L/D=0.2) whose ends are sealed with either (a) PRs or (b) ORs. Lubricant (ISO VG2) flows thru one feedhole at the land middle plane. The supply pressure (and oil flowrate) increase from 0.7 bar(g) to 6.2 bar(g). In the PR-SFD, oil leaves the film land though the rings' abutted ends (PR slits). The OR-SFD effectively seals any leakage; hence, lubricant flows out through a discharge hole at a location halfway of the film (upper) land length.

Multiple sets of single frequency (10 Hz-100 Hz) dynamic loads produced circular centered orbits with amplitude (r) equal to 10% and 30% of the radial clearance (c=0.373 mm). For the PR-SFD, the damping coefficient decreases as the lubricant supply pressure drops, whereas a (large magnitude) added mass coefficient slightly increases. For the-OR SFD, the damping and added mass coefficients do not change with the (albeit small) orbit radii. Both the PR-SFD and O-SFD deliver damping and force coefficients of nearly identical magnitude.

Analysis of recorded film dynamic pressures shows the *peak-peak* pressure increases with both whirl frequency and orbit amplitude. Operation with the lowest supply pressure (0.7 bar) shows the film pressure does not increase above a certain excitation frequency, thus denoting the onset of air ingestion and entrapment, in particular for the PR-SFD.

In other tests, the lubricant flow suddenly stops while the shakers still deliver dynamic loads. The test system response shows a rapid increase in whirl orbit as the squeeze action pushes away the remnant lubricant in the film. The effect is most notable for the PR-SFD that quickly loses its damping ability. The OR-SFD also produces larger orbits yet reaching a limit size, likely due to the O-rings resilience. However, with O-rings as end seals, as soon as the oil flow stops, the orbit jumps to an eccentric position.

Table of Contents

Nomenclature

$a_{\alpha(t),\ (\alpha=X,Y)}$	Acceleration of bearing cartridge [m/s^2]
c	Nominal radial clearance [μm]
$C_{\alpha\beta,\ (\alpha,\beta=X,Y)}$	SFD damping coefficients [N·s/m]
C_S	Dry structure damping coefficient [N·s/m]
D	Journal diameter [m]
e_s	Static eccentricity (along 45º) [m]
$F_{\alpha(t),\ (\alpha=X,Y)}$	Components of the applied dynamic load amplitude [N]
F_s	Static load [N]
f	Excitation frequency [Hz]
f_n	Test system natural frequency [Hz]
$H_{\alpha\beta,\ (\alpha,\beta=X,Y)}$	Measured system complex dynamic stiffness [MN/m]
h	Lubricant film thickness [μm]
i	$\sqrt{-1}$. Imaginary unit
$K_{\alpha\beta,\ (\alpha,\beta=X,Y)}$	SFD stiffness coefficients [N/m]
K_S	Structural support stiffness [N/m]
$K_{S+O\text{-}ring}$	Structural support stiffness [N/m] with O-ring installed
L	Film land length [m]
$M_{\alpha\beta,\ (\alpha,\beta=X,Y)}$	SFD added mass coefficients [kg]
M_S	Dry structure added mass coefficient [kg]
M_{BC}	Bearing cartridge mass [kg]
P	Dynamic pressure in film land [Pa]
P_s	Static oil pressure at inlet [Pa(g)]
Q_s	Lubricant supply flowrate [LPM]
r	Orbit amplitude [m]
R	Journal radius, $R=½D$ [m]
T	Lubricant temperature [ºC]
t	Time [s]
V_s	$=r\omega$. Squeeze film velocity [m/s]
$X,Y,\ \bar{X},\bar{Y}$	Coordinate systems
$x_{(t)},\ y_{(t)}$	Displacement of BC respect to journal along X and Y axes [m]
z	Axial coordinate origin to mid-plane of film land
α_v	Lubricant viscosity coefficient [-]
$\phi_{orifice}$	Diameter of feedhole orifice [m]
$\phi_X,\ \phi_Y$	Phase angles of the fundamental components of the Fourier series built functions from measured displacements along the X, Y axes [rad]
$\rho,\ \mu$	Oil density [kg/m^3] and viscosity [Pa·s]
Θ	Circumferential coordinate [rad]
ω	Excitation frequency ($\omega=2\pi f$) [rad/s]
ζ	Damping ratio [-]

Vectors and matrices

$\bar{\mathbf{a}}_{(\omega)}$	Vector of accelerations $\{a_{X(\omega)},\ a_{Y(\omega)}\}^{\mathrm{T}}$ in the frequency domain [m/s^2]

C	Matrix of damping coefficients
$\bar{\mathbf{e}}_s$	Vector of static eccentricities $\{e_{sX}, e_{sY}\}^{\mathrm{T}}$ [m]
$\bar{\mathbf{e}}_{(t)}$	Vector of dynamic eccentricities $\{x_{(t)}, y_{(t)}\}^{\mathrm{T}}$ [m]
K	Matrix of stiffness coefficients [N/m]
$\bar{\mathbf{F}}_{(\omega)}$	Vector of dynamic loads $\{F_{X(\omega)}, F_{Y(\omega)}\}^{\mathrm{T}}$ in the frequency domain [N]
$\bar{\mathbf{H}}_{(\omega)}$	$\mathbf{K} - \omega^2\mathbf{M} + i\omega\mathbf{C}$ Matrix of dynamic stiffness coefficients in the frequency domain [N/m]
M	Matrix of added mass coefficients [kg]
$\mathbf{Z}_{(\omega)}$	Vector of bearing cartridge displacements relative to a journal in the frequency domain [m]

Subscripts

avg	$\Box_2(XX+YY)$
BC	Bearing cartridge
CCW	Counter Clockwise
CW	Clockwise
Dry	Dry friction
L	Lubricated system
SFD	Squeeze film damper
S	Structure
s	Static

Acronyms

DAQ	Data acquisition
PR	Piston ring
SFD	Squeeze film damper

Introduction

Modern high performance turbomachinery demands high power density with proven efficiency. Squeeze film dampers (SFDs) aid to reduce excessive rotor synchronous vibration, to suppress non-synchronous instabilities, and to isolate a rotor from the stator or housing. Thus, rotating machinery often implements SFDs to traverse safely thru critical speeds and to reduce transmitted forces to the casing [1, 2].

Figure 1 depicts a schematic view of a sealed ends SFD in series with a ball bearing supported rotor. The annular gap between the bearing cartridge and the outer race of a ball bearing makes the lubricant film. An anti-rotation pin (dowel pin) or a centering spring (squirrel cage) prevents rotation of the outer race. SFDs precess due to rotor displacements that squeeze the lubricant film. This film generates a hydrodynamic pressure that produces a reaction force [1].
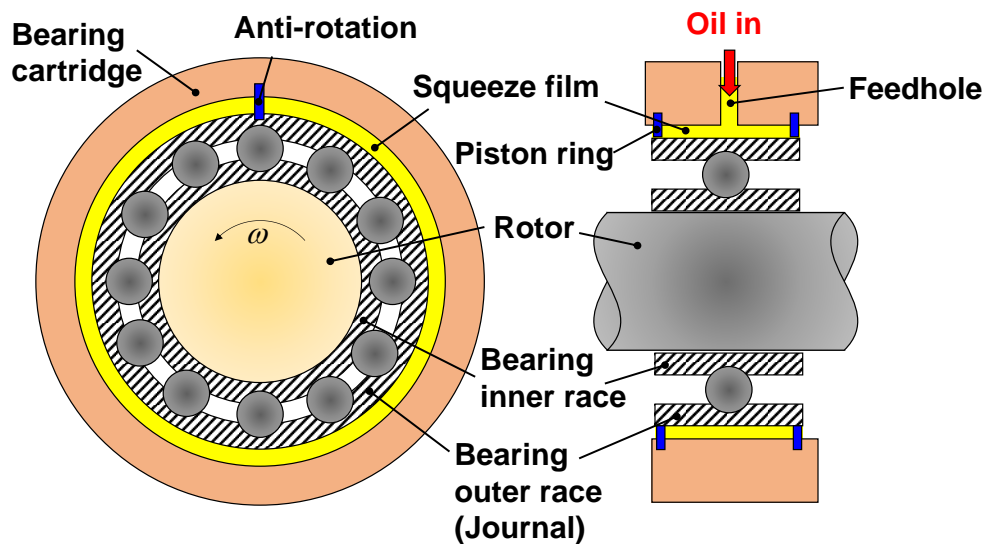

Figure 1. Schematic views of a hole-fed SFD with (piston ring) sealed ends [1].

The damping effect depends on the damper geometry, lubricant physical properties, and operating conditions. Zeidan et al. [3] identify SFD operation with two distinct types of fluid cavitation and a regime due to air ingestion and entrapment. Vapor cavitation appears in tightly sealed ends SFDs when the film pressure reaches vapor pressure. Air ingestion occurs in vented or not tightly sealed ends SFDs operating with a high squeeze velocity and not supplied with sufficient lubricant to fill the clearance.

Literature review

Sealed ends SFDs

Vance and Kirton [4] experimentally investigate the effect of end seals on the generation of film dynamic pressure in a long SFD with L/D=0.96 and c/R=0.0124. The long bearing theory predicts well the pressure field for operating with a circular centered whirl orbit. However, the long bearing theory cannot accurately predict the magnitude of peak-to-peak pressure for operation in neither the laminar flow nor the vortex flow regime. End seals with minimal end leakage result in a negligible pressure variation along the axial direction. During the tests, only one pressure transducer records the film pressure. Hence, the likely pressure distortion due to the lubricant supply line could not be assessed properly.

Feder et al. [5] present experimental and analytical investigations on the dynamic force generated by a sealed ends SFD operating with circular centered whirl orbits. O-ring seals installed on the sides of the damper prevent leakage thru the ends. Hence, the analytical model uses the long bearing theory. The test journal (D=163.6 mm and L=50.8 mm)describes orbits with radius r/c=0.2-0.8 (c=508 μm) and over a frequency range ω=8.3-53.3 Hz. A thick lubricant with viscosity μ~25.5 cPoise supplies is delivered with supply pressure P_s=0.7-5.6 bar thru two feedholes with diameter of 0.8 mm and located in a smaller annular groove. A lubricant discharge hole (diameter of 0.8 mm) locates at another axial end of the film. For P_s<3.8 bar, the π-film model predicts well the radial and tangential forces for operation with r/c<0.6, albeit the model over-predicts forces for operation with r/c>0.6. The predicted tangential force from the full-film model matches well the measurements, whereas the predicted radial force does not. For P_s>3.8 bar, the predicted force from the full-film model agrees with the measurements. Further increase in the supply pressure does not produce any noticeable change in damper force. Later, Bansal and Hibner [6] extend the work in Ref. [5] and present results for statically off-centered (eccentric) whirl orbits. The measurements and predictions of pressure distribution and film forces show significant discrepancy, likely due to ignoring fluid inertia effects in the model.

Marmol and Vance [7] present an analysis to predict the effect of an end seal on the leakage and dynamic performance of SFDs. The authors define boundary conditions for

distinct end seal configurations including a piston ring (PR), a radially installed O-ring, and an axially placed O-ring. The analysis results closely match test data from four damper test rigs, sealed ends or open ends. The PR seals with a large leakage (19 cm^3/s) have negligible effect on the squeeze film pressure. However, O-ring seals with a tight clearance effectively restrict axial flow. The long bearing model is valid only for specific end seal configurations. The predicted pressure distribution solely depends on the side leakage, not the actual seal type.

Miyachi et al. [8] present experimental damping force coefficients for a short-length SFD (L/D=0.2) with distinct sealing mechanisms, i.e., piston ring seals, O-ring seals, and end grooves (open). Tests are conducted in a damper having distinct clearance ratios (c/R)= 0.4 %, 0.2 % and 0.1 . As the oil supply pressure increases from 1 bar to 4 bar, the damping coefficients for the PR sealed ends SFD nearly double, whereas the damping coefficients for the O-ring sealed ends SFD stay relatively constant. The authors note that the discrepancy is likely due to an increased (sliding) friction between the sidewalls of the PRs and the damper walls as the oil supply pressure increases.

Lund et al. [9] present an analysis for finite length SFDs with end seals and a perturbation method to calculate inertia and damping force coefficients from circular whirl orbits. The authors report that damping coefficients delivered by the short length bearing theory with a small leakage flow are ~28% of those predicted by the long bearing model. Note the authors assume the lubricant supplies thru a central groove and at fixed supply pressure. The model does not include the effects of an inlet feedhole or a discharge hole as a lubricant supplies thru an annular center groove with a fixed supply pressure.

San Andrés and Vance [10] show the importance of fluid inertia on the performance of sealed ends SFDs. The authors introduce a leakage factor to account for the side flow in a PR sealed ends damper. Jung and Vance [11] compare predictions of force coefficients and pressure distribution with test data. The journal has L= 23.9 mm and D=127 mm with clearance c=1.6 mm (L/D=0.25). End grooves at the end of the journal are sealed with serrated PRs, which aim to prevent distortions of the hydrodynamic pressure. A long bearing solution modified with the side leakage factor agrees with the

test results. Kim and Lee [12] advance further analysis to predict the force coefficients of a sealed ends SFD with a central feed groove that acts as a dynamic compliance.

Levesley and Holmes [13] compare the experimental performance of a SFD (*L/D*=0.1 and *c/R*=0.003) with two sealing arrangements, one with piston ring seals and another one with end plates seals. The authors discover that a reduction in lubricant supply (hence also flowrate) does not significantly affect the performance of the PR sealed ends damper, which generates much higher damping than an end plate sealed ends damper. This is likely due to the difference between flow conductances of the end seals.

Arauz and San Andrés [14] experimentally quantify the effects of whirl frequency and lubricant viscosity on the film dynamic pressures and the force response of an open end SFD and a partially sealed ends SFD. The test journal diameter *D*=129.4 mm with length *L*=26.4 mm (*L/D*=0.2) and radial clearance *c*=0.381 mm. The journal is off-centered with e_s/*c*=0.25. A SAE 30 engine oil flows into the film thru a feedhole at the top of the journal; the oil supply pressure P_s=3.1-5.5 bar and the flowrate Q_s=1.0-1.4 LPM. One axial end of the damper section is open and the other is sealed with a PR. The SFD journal performed circular orbits with frequency ranging ω=33 Hz-83.3 Hz. The partially sealed configuration produces larger damping than the open ends SFD. At a high frequency (>67 Hz), lubricant cavitation occurs in both damper configurations. After, the rate of increment of the squeeze film force decreases with an increase in frequency decreases.

De Santiago and San Andrés [15] evaluate the effectiveness of integral dampers with end gap seals (clearance =0.127, 0.102 and 0.076 mm) in ameliorating the imbalance response of a test rotor. Damping coefficients are determined from the peak rotor response due to a mass imbalance when crossing a first critical speed. The tests demonstrate that end gap seals substantially increase the system viscous damping coefficient by restricting axial flow through the film lands. However, a too tightly sealed damper offers a limited improvement in damping capability because the lubricant viscosity decreases as the film temperature increases.

Della Pietra and Adiletta [16] critically review the major findings in SFD research and applications over a 40 year period, from 1960 to 2000. This vital paper, a though

San Andrés and Seshagiri [17] experimentally characterize the dynamic force performance of a centrally grooved SFD with piston rings seal. Two journals A and B with *L/D* of 0.2 (*c/R*=0.0022) and 0.1 (*c/R*=0.00217) are used. The test results are compared with those of an open ends damper. The piston ring seals effectively restrict oil leakage to produce a larger film dynamic pressure than in an open ends damper; the same goes for significant increments in damping and added mass coefficients. Predictions from a modern computational model (orbit based) agree well with the experimental force coefficients.

Recently, Jeung and San Andrés [18] perform single frequency dynamic load tests, sine-sweep dynamic load tests, and single impact load tests to quantify the dynamic response of an open ends and a piston ring sealed ends short length (*L/D*=0.2) SFD with clearance of ~0.254 mm (*c/R*=0.004). The authors experimentally characterize the flow conductance for both the open ends and sealed ends SFD. For single frequency dynamic load tests, the direct damping coefficient for the sealed ends SFD is 11-13 times greater than that of the open ends SFD, whereas the direct added mass coefficient is 11 times greater.

This report presents comprehensive experimental results assessing the effect of lubricant supply pressure (and flowrate) on the forced response of a SFD with two types of end seals (piston rings and O-rings). Appendix E details the effect of sudden loss of supply flow on dynamic performance of the test damper.

Description of the Experimental Facility and Test Damper

Figure 2 depicts a photograph and a schematic top view of the SFD test rig consisting of a bearing test stand, two orthogonally placed electromagnetic shakers (max. 2,450 N), and a hydraulic static loader located 45° away from the shakers. The shakers connect to the bearing cartridge via slender stingers. The static loader pulls the bearing cartridge to various static eccentric positions with respect to the journal fixed center. Both the SFD test stand and the shakers are secured to a table on anti-vibration mats to attenuate transmitted forces to the table.

The SFD test bearing consists of a rigid pedestal, journal base, support rods, journal, and bearing cartridge (BC). The journal base bolts onto the pedestal, which is mounted to the table. Four elastic steel rods provide a structural stiffness of 1.6 MN/m[1] and the BC has effective mass M_{BC}= 15 kg.
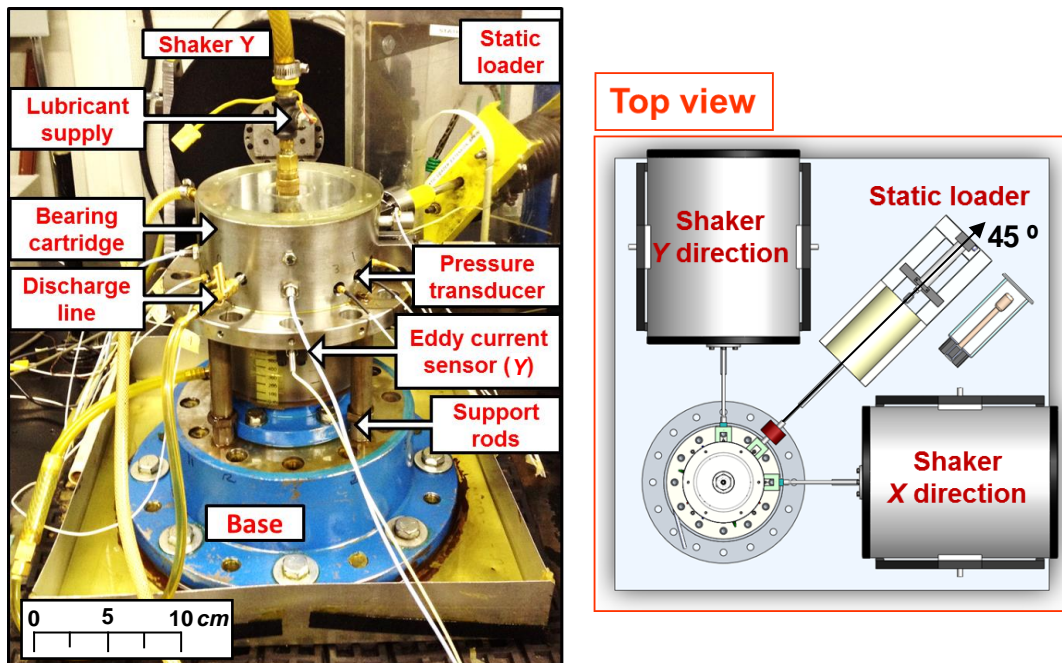

Figure 2. Photograph and top view of SFD test rig with electromagnetic shakers and static loader.

---

[1] The structural stiffness is smaller than the one measured in 2016 [18] since the bolts fixing four support rods have loosened due to many number of tests with high frequency and large amplitudes of excitation force. Presently, the bolts are retightened and K_s~6 MN/m [May, 2017].

Figure 3 shows a photograph of the test journal and a schematic view with detail dimensions. Table 1 lists the journal dimensions and lubricant properties. The short length SFD (L/D=0.2) has a film land length L=25.4 mm, diameter D=127 mm, and a radial clearance c=0.373 mm (c/R=0.006). Two end grooves, each with width 2.5 mm and depth 3.8 mm, host either piston rings (PRs) or O-rings. The journal end lips have a width equal to 3.3 mm. The journal has one feedhole (θ=45º) at the film mid-plane (z=0) with diameter $\phi_{orifice}$ of 2.5 mm.

A hydraulic pump supplies a mineral oil to the journal film land thru the feedhole. The lubricant ISO VG2 has density ρ=820 kg/m^3 and kinematic viscosity μ=2.57 cPoise at 23º C. Both physical properties are comparable to those of lubricants used in aircraft engines operating at high temperature (T~200ºC). Appendix A details the measured viscosity and density of the lubricant.
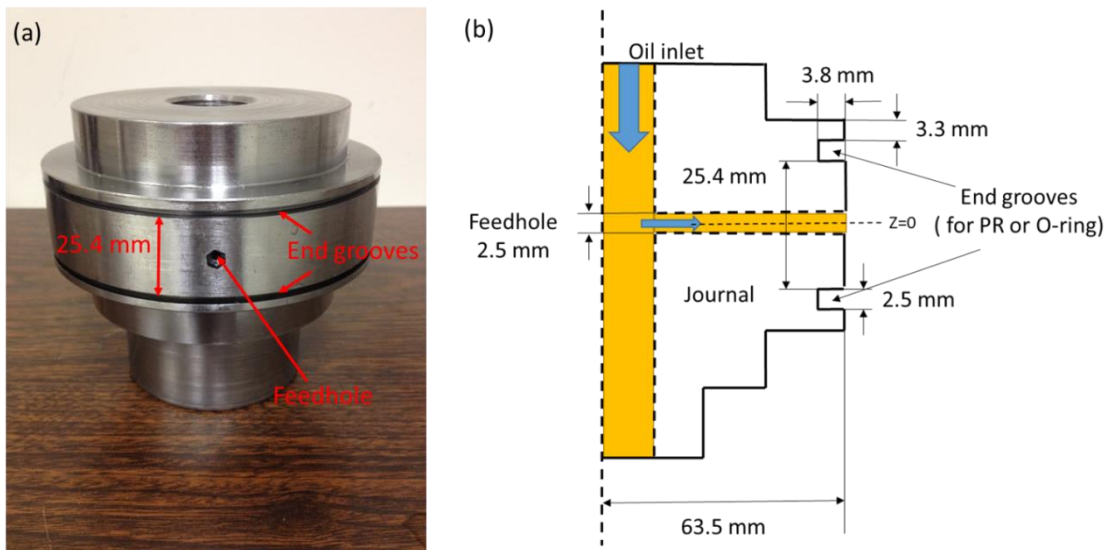

Figure 3. (a) Photograph of journal (Material: AISI 1018 carbon steel) – see end grooves, and (b) cross section of journal (drawing not to scale and certain features are exaggerated).

Table 1. Dimensions and lubricant properties of test SFD

Journal diameter, D	127 mm
Nominal axial film land length, L	25.4 mm
Nominal radial clearance, c	373 µm
Feedhole orifice diameter, $\phi_{orifice}$	2.5 mm
Feedhole location, θ	45°
End groove width	2.5 mm
End groove depth	3.8 mm
Lubricant	ISO VG2
Lubricant viscosity at supply temperature, μ	2.57 mPa-s
Lubricant density, ρ	820 kg/m^3
Supply temperature	23 °C
Structural stiffness, K_S	1.6 MN/m
Bearing cartridge mass, M_{BC}	15 kg
Calculated structural natural frequency, ω_n	51 Hz

Figure 4 shows photographs of (a) a PR and (b) an O-ring as well as schematic views of the SFD with (c) PR sealed ends, and with (d) O-ring sealed ends. When closed, the PR outer diameter contacts the ID of the BC (127.16 mm). For the tests with PRs, each piston ring slit (abutted ends) locates at θ=135°. Upon installation, the lubricant fluid flows through the piston ring slit; the flow area is ~4.19×10^{-4} mm^2.

For the O-ring sealed SFD, the groove depth is adjusted by using a steel spacer, a zinc galvanized carbon steel wire with its diameter of 1.5 mm. The O-ring used is a multipurpose Buna-N O-ring with an outer diameter of 120 mm and a thickness of 2.6 mm (AS568 standard O-ring size number 158). Note that the lubricant in the O-ring sealed ends SFD does not leak thru the axial sealed ends[2], but discharges through an orifice hole of diameter 2.0 mm at θ=240° and $z = \frac{1}{4}L$.

---

[2] For an O-ring sealed SFD without a discharge hole, the pressure quickly builds up in the film land and the oil supply line as the upstream pump keep pushing more lubricant into the SFD. A relief valve in the supply line opens at a set pressure of ~7 barg.

For an inlet pressure, ~689 kPa, the flowrate thru the O-ring sealed SFD (19 cm^3/s) is larger than that for the PR sealed SFD (13 cm^3/s). Appendix D details the whole set of flow measurements versus supply pressure (P_s=0.7-6.2 barg).
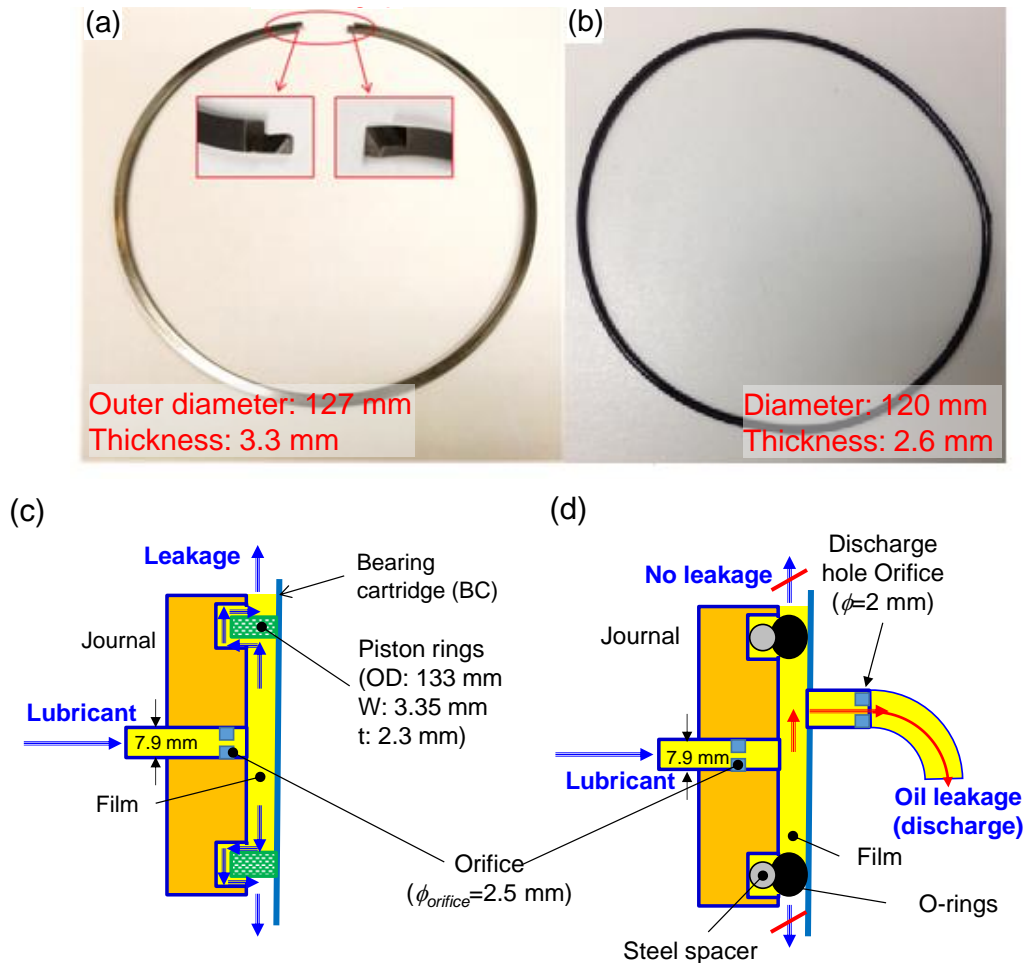

Figure 4. Photographs of end seals and schematic views of their installation: (a, c) piston rings, and (b, d) O-rings. The O-ring seal stretches when installed in a journal groove.

Description of Tests with Single Frequency Dynamic Loads[3]

Figure 5 provides (a) a description of the BC kinematics for a whirl orbit motion, (b) the coordinate systems of the BC and a static loader and (c) a depiction of various whirl orbits at centered and off-centered conditions. Figure 5 (a) depicts the whirl motion of the BC with amplitude components (r_X, r_Y) at a frequency $\omega_{(t)}$. $\vec{\mathbf{e}}_s$ and $\vec{\mathbf{e}}_{(t)}$ denote the static and dynamic eccentricity vectors from the origin to the BC static position, and the origin to the orbital path, respectively. As shown in Figure 5(b), the static loader pulls the BC to a static off-centered ($\vec{\mathbf{e}}_s$) condition along the $\overline{X}$ axis, $45°$ away from (X, Y).

For whirl orbit motions, the experiments include single-frequency dynamic load excitations. The dynamic loads exerted by the shakers along the X and Y directions are

$$\mathbf{F}_{CW} = F\begin{bmatrix} \cos(\omega t) \\ \sin(\omega t) \end{bmatrix}; \mathbf{F}_{CCW} = F\begin{bmatrix} \cos(\omega t) \\ -\sin(\omega t) \end{bmatrix} \tag{1}$$

where F is a load magnitude and ω represents excitation frequency. Subscripts CW and CCW denote clockwise and counter-clockwise motions that correspond to two linearly independent excitations force vectors.

For single-frequency dynamic loads, the excitation frequency ω is constant with magnitude set at steps of 10 Hz over the frequency range 10-120 Hz. The shaker load limit (2,450 N) prevents tests with a too large whirl amplitude and at a too high frequency as the damper reaction force would be too large.

The test rig is modeled as a two degree of freedom mechanical system and governed by the following equation of motion in the frequency domain

$$\left[\mathbf{K}_L - \omega^2 \mathbf{M}_L + i\omega \mathbf{C}_L \right] \mathbf{Z}_{(\omega)} = \mathbf{F}_{(\omega)} - M_{BC}\mathbf{a}_{(\omega)} \tag{2}$$

where $\mathbf{F}_{(\omega)}$, $\mathbf{Z}_{(\omega)} = \{X, Y\}^T$, $\mathbf{a}_{(\omega)}$ are vectors in X and Y directions of the discrete Fourier transforms of the recorded dynamic load, bearing cartridge (BC) displacement relative to the journal, and BC acceleration, respectively. $M_{BC} \sim 15$ kg is the mass of the BC.

Discrete Fourier transforms of the data obtained from two linearly independent excitation force vectors $\mathbf{F}_{CW}$ and $\mathbf{F}_{CCW}$ produce:

$$\mathbf{F}_{CW} \Rightarrow \begin{Bmatrix} \mathbf{Z}_{CW} \\ \mathbf{a}_{CW} \end{Bmatrix}, \mathbf{F}_{CCW} \Rightarrow \begin{Bmatrix} \mathbf{Z}_{CCW} \\ \mathbf{a}_{CCW} \end{Bmatrix} \tag{3}$$

---

[3] Portions of this section reproduce ad-verbatim information presented in [18] .
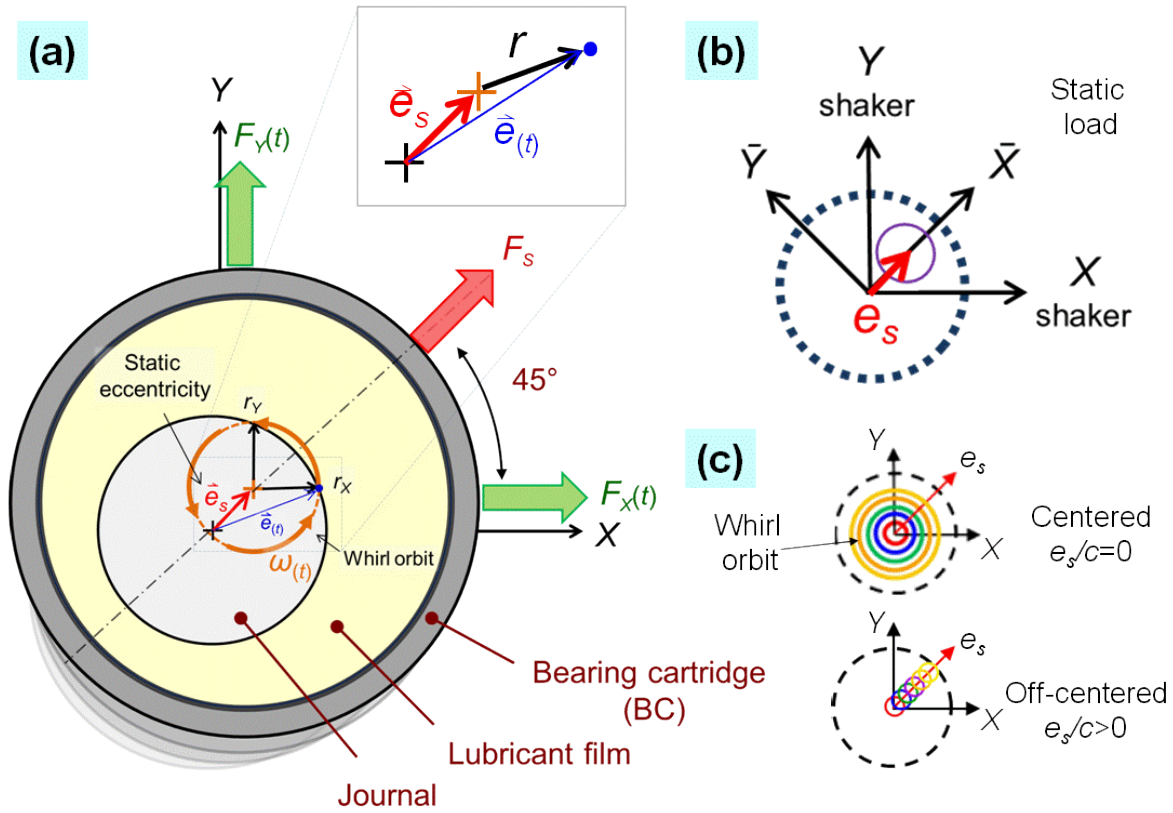
Figure 5. (a) Schematic view of whirl orbit kinematics (Exaggerated film clearance for illustrative purposes), (b) coordinate systems for motion, (c) various orbits with amplitude (*r*) at centered and off-centered conditions (*e*$_s$) [18].

To identify the lubricated system force coefficients $(\mathbf{K}, \mathbf{C}, \mathbf{M})_L$, a complex dynamic stiffness matrix is defined as

$$\mathbf{H}_L = \left[\mathbf{K} - \omega^2 \mathbf{M} + i\omega \mathbf{C}\right]_L \tag{4}$$

From Eqns. (2) and (3)

$$\mathbf{H}_L = \left[\mathbf{F}_{CW} - M_{BC}\mathbf{a}_{CW} \quad \mathbf{F}_{CCW} - M_{BC}\mathbf{a}_{CCW}\right]\left[\mathbf{Z}_{CW} \quad \mathbf{Z}_{CCW}\right]^{-1} \tag{5}$$

The real part $\mathrm{Re}(\mathbf{H}_L) \rightarrow (\mathbf{K}_L - \omega^2 \mathbf{M}_L)$ yields the lubricated system stiffness $(\mathbf{K}_L)$ and added mass $(\mathbf{M}_L)$ coefficients, and the imaginary part $\mathrm{Im}(\mathbf{H}_L) \rightarrow (\omega \mathbf{C}_L)$ yields the lubricated system damping coefficients $(\mathbf{C}_L)$.

The SFD complex stiffness matrix $\mathbf{H}_{SFD}$ follows by subtracting the dry system complex stiffness $(\mathbf{H}_S)$, identified in the same manner, from the lubricated system complex stiffness. That is

$$\mathbf{H}_{\text{SFD}} = \mathbf{H}_{\text{L}} - \mathbf{H}_S \qquad (6)$$

Test SFD cross-coupled complex stiffness coefficients (H_{XY}, H_{YX}) are at least one order of magnitude smaller than the direct coefficients (H_{XX}, H_{YY}). These small cross-coupled stiffness coefficients are negligible and not discussed here. See Appendix F for more details.

Appendix B details the identification of mechanical parameters $(K, C, M)_S$ for the test dry system. In brief, the estimated structural force coefficients for the dry system (without lubricant in the film land) are K_S=1.6 MN/m, M_S=1.9 kg, and C_S=0.65 kN.s/m.. The dry system natural frequency is $\omega_n = \sqrt{\dfrac{K_S}{M_{BC} + M_S}}$ =51 Hz. The (dry system) damping ratio (ζ) equals 0.06 and 0.08 along the X and Y directions.

Experimental Results

This section presents the experimental results obtained from circular centered whirl motions conducted with the sealed ends SFDs. The shakers exert single frequency dynamic forces to produce circular whirl motions of the BC with amplitude r=0.1c and 0.3c. During the experiments, the lubricant supply pressure P_s ranges from 0.7 bar to 6.2 bar. A decrease in supply pressure corresponds to a decrease in lubricant flow rate.

For the PR sealed ends damper describing orbits with radius r/c=0.3, Figure 6 shows the real and imaginary parts of the lubricated system dynamic stiffness, Re(H_{XX}, H_{YY})$_L$, Im(H_{XX}, H_{YY})$_L$, as well as the physical fit model. The lubricant supply pressure varies from 1.4 bar to 6.2 bar. The inset table lists the SFD direct force coefficients (K, C, M)$_{XX,YY}$ and the curve fit correlation factor to the KCM model. The correlation factor R^2>0.95 shows that the KCM model fits well the measured coefficients (H_{XX}, H_{YY}). In lubricant theory, SFDs do not have stiffness coefficients, i.e. reaction forces due to static journal displacements. However, the measurements reveal stiffnesses (<1.0 MN/m), most likely due to (a) the asymmetric pressure field induced by both the feedhole and the PR slits, and (b) the uncertainty of the measured stiffness.
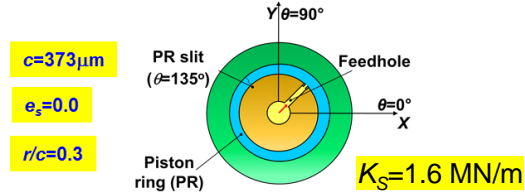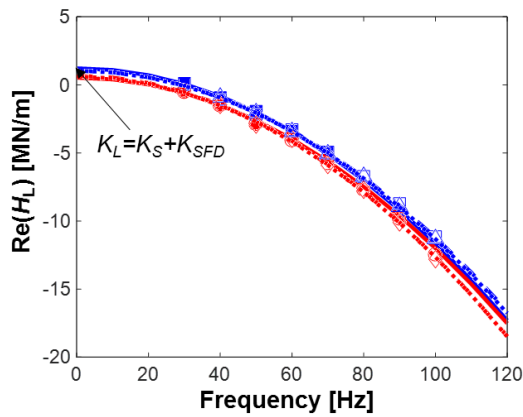
For the PR sealed ends SFD, Re(H_{XX}, H_{YY})$_L$ show a downward parabolic curve, indicating positive added mass coefficients M_{XX} and M_{YY}. Im(H_{XX}, H_{YY})$_L$ linearly increase as the frequency (ω) increases, thus evidencing that a viscous type damping is dominant,

i.e., $\mathrm{Im}(H_{XX}, H_{YY}) \sim \omega(C_{XX}, C_{YY})$. The slope for $\mathrm{Im}(H_{XX}, H_{YY})_L$ increases as the supply pressure increases, thus indicating the damping coefficients (C_{XX}, C_{YY}) increase. The added inertia coefficients (M_{XX}, M_{YY}) remain at a constant ~29 kg with an increase in the lubricant supply pressure (P_s).
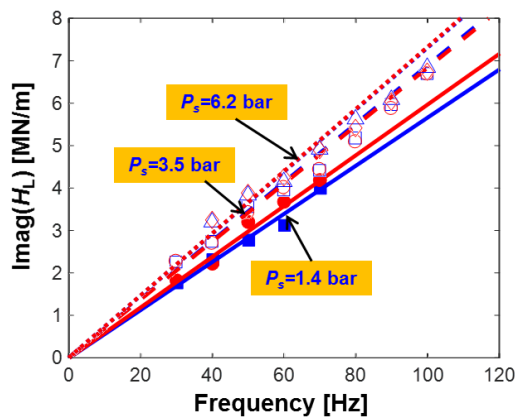
Similarly, for the O-ring sealed ends SFD, Figure 7 displays the real and imaginary parts of $\mathbf{H}_L$ and the fit models for circular centered orbit motions (r/c=0.3) and excitation frequency range ω=10-100 Hz. The lubricant supplies thru one feedhole at θ=45º with supply pressure (P_s) varying from 2.1 bar to 6.2 bar. The discharge hole locates at θ=240º (30º away from the Y-axis) and it may cause orthotrophy of the coefficients, $H_{XX} \neq H_{YY}$. Damping coefficients slightly increase as P_s increases. Meanwhile, the real part of H indicates that the inertia coefficients slightly decrease as the supply pressure increases.

The damping coefficients for the O-ring sealed ends SFD are larger than those for the PR sealed ends SFD. This is because the O-rings provide a perfect seal at the two ends of the damper, whereas the PRs allow for leakage through the slits (abutted ends). The added mass coefficient M_{XX} for the O-ring sealed ends SFD is 19% higher than that of the piston ring sealed ends SFD. Similarly, M_{YY} is 13% smaller than M_{YY} for the PR sealed SFD. The difference is likely due to the discharge port being closer to the Y-axis rather than to the X-axis. Note the PR slit area (abutted area) locates between the X and Y-axes (θ=135º) is much smaller than the area of the discharge hole.

The stiffness coefficients (K_{XX}, K_{YY}) for the O-ring sealed SFD are also larger than those for the PR sealed ends SFD ($K_{s+O\text{-}ring}$=2.2 MN/m > K_s). See Appendix B for more details. This is because the O-rings provide an additional stiffness due to their own elasticity (compliance).
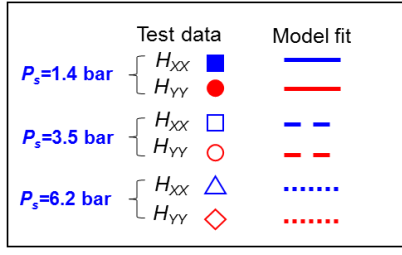
Figure 6. PR sealed ends damper (*c*=373 μm): Real and imaginary parts of direct complex stiffness for lubricated system (H_{XX}, H_{YY})$_L$ vs. whirl frequency. Circular centered orbits with radius *r/c*=0.3 (e_s=0). Whirl frequency range ω= 10-100 Hz. Lubricant supplies thru a feedhole at θ=45° with supply pressure P_s=1.4, 3.5, and 6.2 bar. PR slits locate at θ=135°.

Re(H_L) [MN/m]

P_s=3.5 bar

P_s=6.2 bar

$K_L=K_{S+O\text{-}ring}+K_{SFD}$

P_s=2.1 bar

Frequency [Hz]

Imag(H_L) [MN/m]

P_s=6.2 bar

P_s=3.5 bar

P_s=2.1 bar

Frequency [Hz]

c=373μm

e_s=0.0

r/c=0.3

Y θ=90°

O-ring

θ=0°

X

Discharge hole
(ϕ=2.0 mm)
Z=L/4

$K_{S+Oring}$=2.2 MN/m

P [bar]	ω [Hz]	Damping C_{SFD} [kN-s/m]		Inertia M_{SFD} [kg]		Stiffness K_{SFD} [MN/m]		Flow Rate [LPM]
		XX	YY	XX	YY	XX	YY	
2.1	30-90	11.4	9.3	38.3	25.1	0.8	-0.3	2.4
3.5	30-90	10.6	9.1	34.5	25.8	-0.4	-0.5	3.8
6.2	40-90	11.0	9.6	31.7	23.4	-0.1	0.0	4.9

P [bar]	ω [Hz]	Correlation coefficient			
		R^2-Re(H_{XX})		R^2-Im(H_{XX})	
		XX	YY	XX	YY
2.1	30-90	0.99	0.99	0.95	0.98
3.5	30-90	1.00	1.00	0.91	0.94
6.2	40-90	1.00	1.00	0.94	0.94

Test data   Model fit

P_s=2.1 bar H_{XX} ■ H_{YY} ●

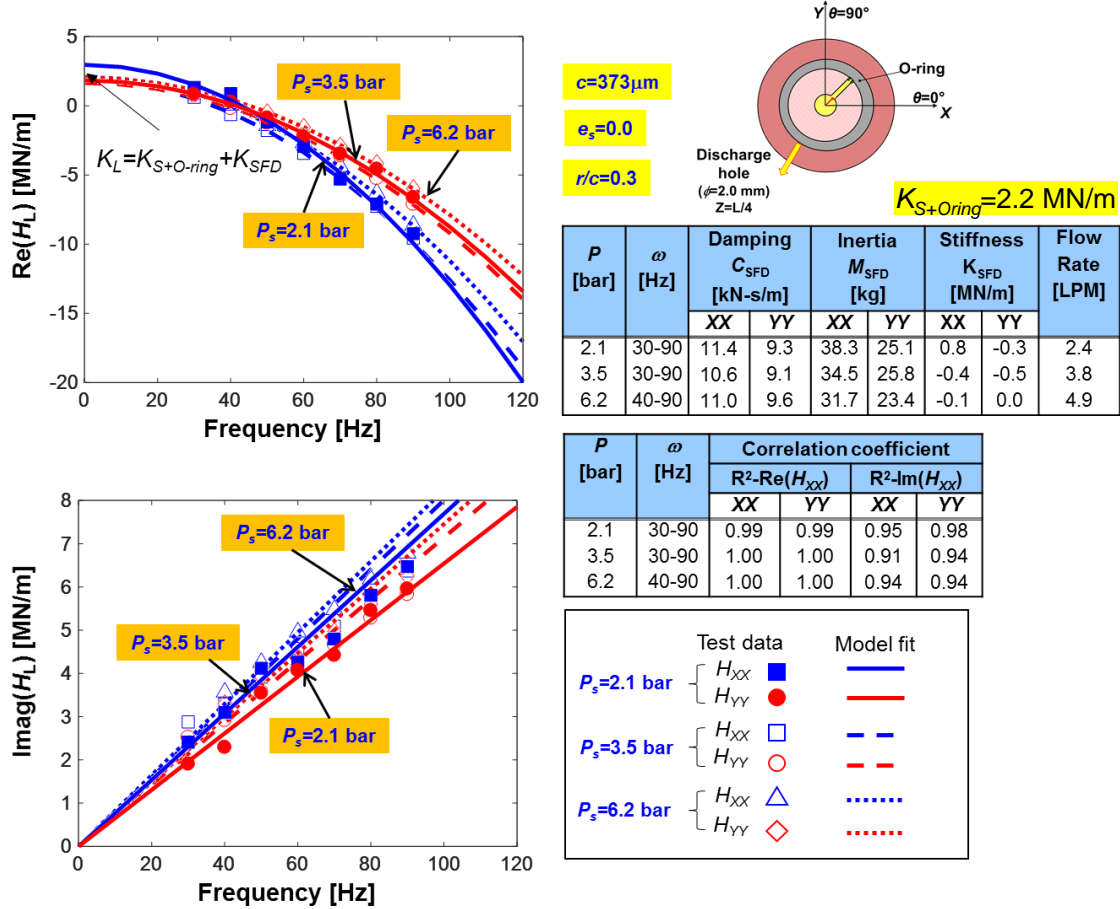P_s=3.5 bar H_{XX} □ H_{YY} ○

P_s=6.2 bar H_{XX} △ H_{YY} ◇

Figure 7. O-ring sealed ends damper (c=373 μm): Real and imaginary parts of direct complex stiffness for lubricated system (H_{XX}, H_{YY})$_L$ vs. whirl frequency. Circular centered orbits with radius r/c=0.3 (e_s=0). Whirl frequency range ω= 10-100 Hz. Lubricant supplies thru a feedhole at θ=45° with supply pressure P_s=2.1, 3.5, and 6.2 bar. A discharge hole diameter of 2.0 mm locates at θ=240° and z = ¼ L.

For the piston ring sealed ends SFD, Figure 8 shows the estimated damping $C_{avg}=\frac{1}{2}(C_{XX}+C_{YY})_{SFD}$ and added mass $M_{avg}=\frac{1}{2}(M_{XX}+M_{YY})_{SFD}$ coefficients versus lubricant supply pressure.[4] The orbit radius is r/c=0.3 and the whirl frequency range is ω=10-100 Hz. C_{avg} increases 30% as the supply pressure increases from 2.1 bar to 6.2 bar whereas M_{avg} stays relatively constant. In this figure and the following ones, the bars denote the experimental uncertainty.

For the O-ring sealed ends SFD, Figure 9 shows the estimated (a) damping $C_{avg}=\frac{1}{2}(C_{XX}+C_{YY})_{SFD}$ and (b) added mass $M_{avg}=\frac{1}{2}(M_{XX}+M_{YY})_{SFD}$ coefficients versus lubricant supply pressure P_s. The orbit radii are r/c=0.1 and 0.3, and whirl frequency ranges from 10 to 100 Hz.

For whirl motions with r/c=0.3, C_{avg} increases ~11% as P_s increases from 2.1 bar to 6.2 bar, whereas M_{avg} decreases ~13%. For motions with r/c=0.1 and P_s>1.4 bar, the damping and inertia coefficients remain approximately constant at ~11 kN-s/m and 30 kg, respectively. For $P_s \leq$1.4 bar, C_{avg} decreases as P_s reduces, whereas M_{avg} remains constant. The effect of the supply pressure is more evident for the tests with the largest orbit size, r/c=0.3.

Figure 10 compares the effect of a change in supply pressure (P_s) on the force coefficients of the PR sealed ends damper and the O-ring sealed ends damper. The data corresponds to circular centered orbits with r/c=0.3. M_{avg} remains at ~30 kg as the supply pressure decreases. C_{avg} for the O-ring sealed ends SFD is approximately 11% larger than C_{avg} for the PR sealed ends damper. However, for both sealed ends dampers, the damping coefficient C_{avg} decreases as P_s drops.

---

[4] For orbits with r/c=0.1, the test with PR sealed ends SFD show a significant contribution of sliding friction or stick-slip effect between the PR seals and the groove surface. Thus, the linear KCM model does not fit into the measurements (R^2<<1). See Appendix G for more details.
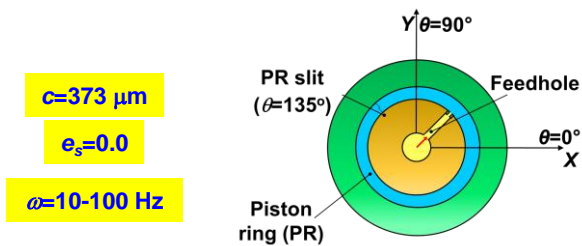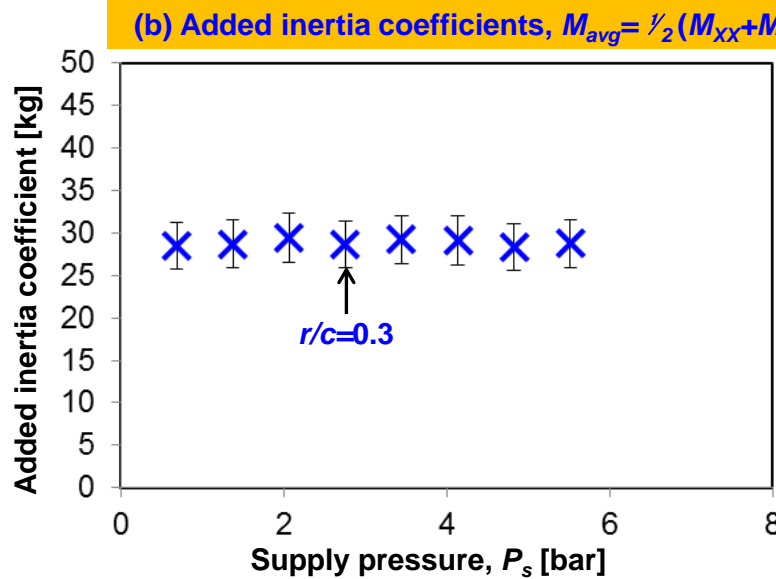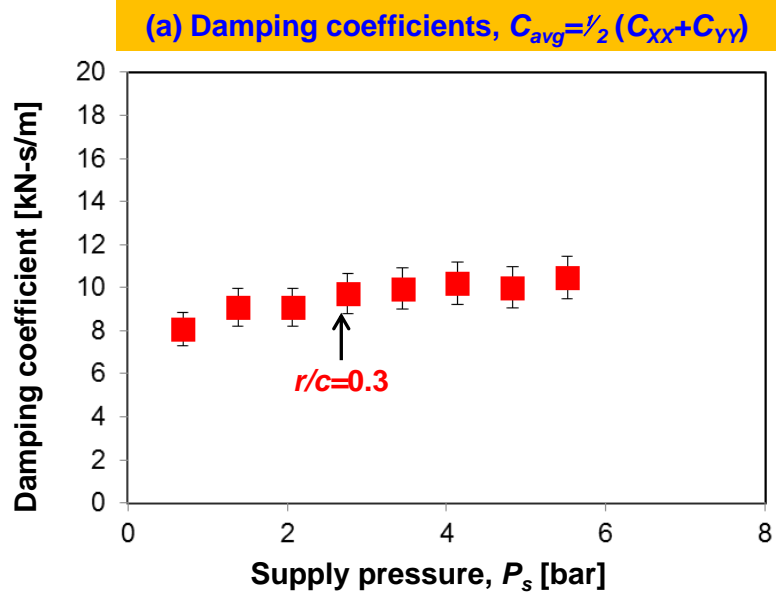
Figure 8. Piston ring sealed ends damper ($c=373$ μm): SFD direct (a) damping C_{avg} and (b) added inertia M_{avg} coefficients vs. lubricant supply pressure. Whirl frequency range ω=10-100 Hz. Circular centered orbits with radius r/c=0.3 (e_s=0). Lubricant supplies thru a feedhole diameter of 2.3 mm at θ=45°.

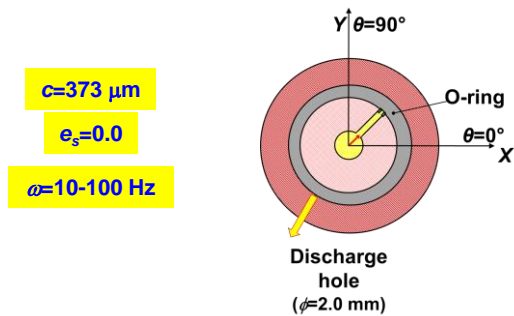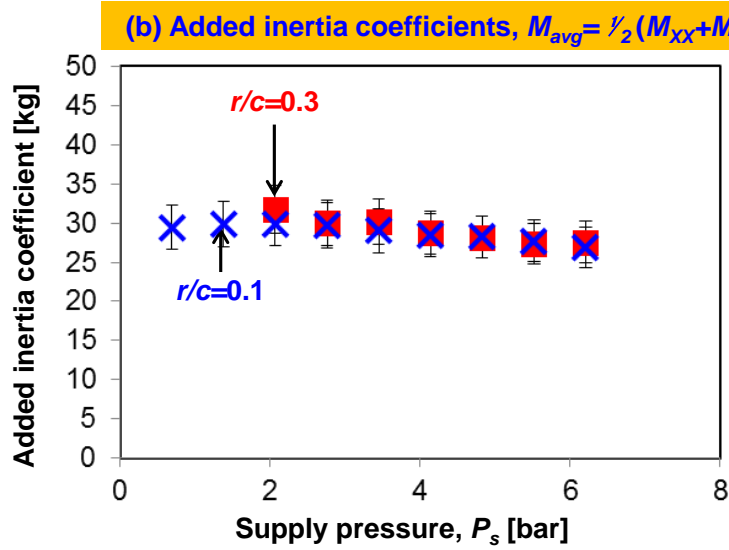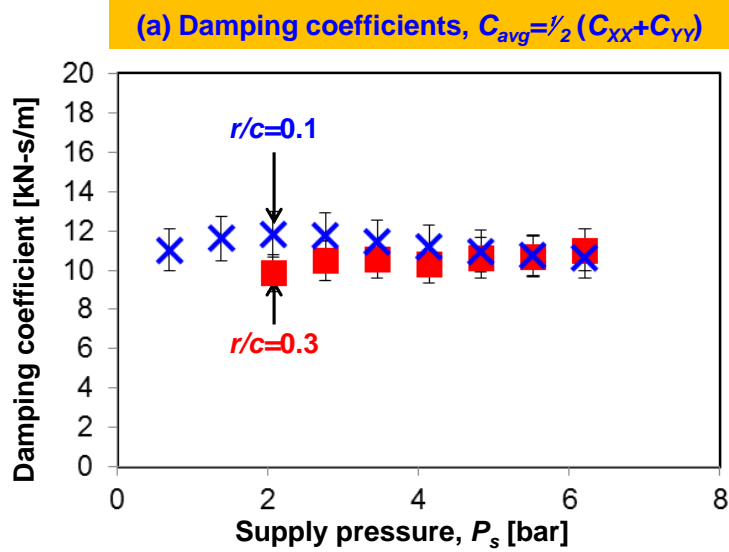**(a) Damping coefficients, $C_{avg} = \frac{1}{2}(C_{XX} + C_{YY})$**

r/c=0.1

r/c=0.3

Damping coefficient [kN-s/m]

Supply pressure, P_s [bar]

(b) Added inertia coefficients, $M_{avg} = \frac{1}{2}(M_{XX} + M_{YY})$

r/c=0.3

r/c=0.1

Added inertia coefficient [kg]

Supply pressure, P_s [bar]

c=373 μm

e_s=0.0

ω=10-100 Hz

Y θ=90°

O-ring

θ=0°

X

Discharge hole (ϕ=2.0 mm)

Figure 9. O-ring sealed ends damper (c=373 μm): SFD direct (a) damping C_{avg} and (b) added inertia M_{avg} coefficients vs. lubricant supply pressure. Circular centered orbits with radii r/c=0.1 and 0.3 (e_s=0) and frequency ω=10-100 Hz. Lubricant supplies thru a feedhole diameter of 2.3 mm at θ=45° and discharges thru a hole with diameter of 2.0 mm at θ=240° and z=¼ L.
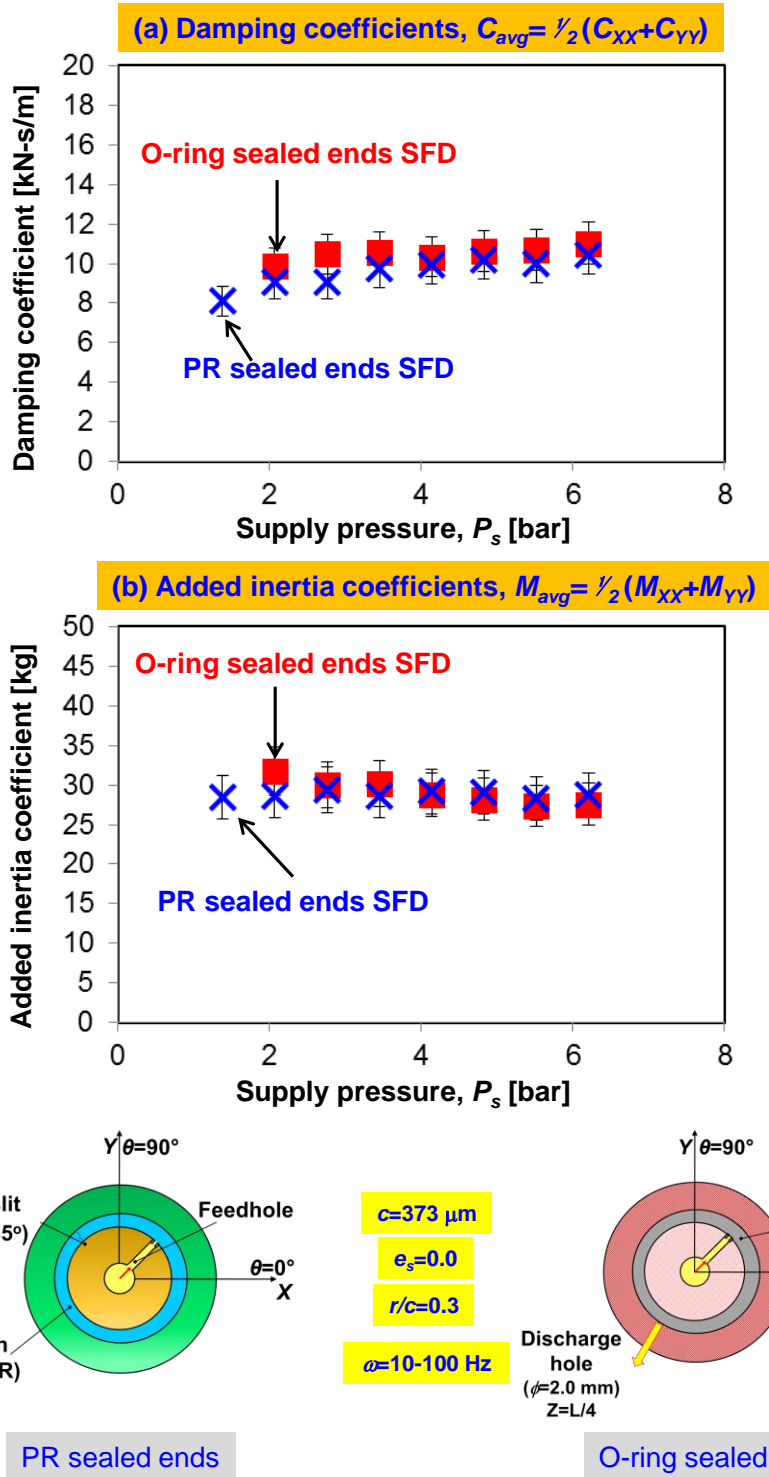
Figure 10. PR sealed ends SFD vs. O-ring sealed ends damper (c=373 μm): SFD direct (a) damping C_{avg} and (b) added inertia M_{avg} coefficients vs. lubricant supply pressure. Circular centered orbits with radius r/c=0.3 (e_s=0), whirl frequency range ω=10-100 Hz. Lubricant supplies thru a feedhole diameter of 2.3 mm at θ=45°.

Comparison of Recorded Film Pressures for PR Sealed Ends Damper and O-ring Sealed Ends Damper[5]

Figure 11 shows the position of pressure sensors in the bearing cartridge (BC). Eight PCB® piezoelectric dynamic pressure sensors ($P_1 - P_8$) and two strain gauge EPX® absolute pressure sensors (E_1 and E_2) are installed in the BC around its circumference. Two sets of three PCB pressure sensors ($P_{1-3} - P_{4-6}$), spaced apart by 90º, record the dynamic pressure at the top, bottom, and mid sections of the damper film land. Note that P_{1-2-3} and P_{4-5-6} are spaced 15º apart. Two other piezoelectric pressure sensors (P_7 and P_8) measure the film dynamic pressures in the end grooves at the exit of the squeeze film land. Note that the pressure sensor tips are flushed with the inner surface of the BC.

This section presents measured pressure profiles in the film lands during test with circular centered orbit motion as well as an analysis of the film dynamic pressures as a function of the amplitude (r) and whirl frequency (ω) of the test damper. Ref. [18] give further details on the film dynamic pressure measurement as a function of amplitude (r) and whirl frequency (ω). The figures in this section depict the *peak-to-peak* dynamic film pressures for the piston ring sealed ends and the O-ring sealed ends damper configurations.

---

[5] Portions of this section reproduce ad-verbatim information presented in [18].
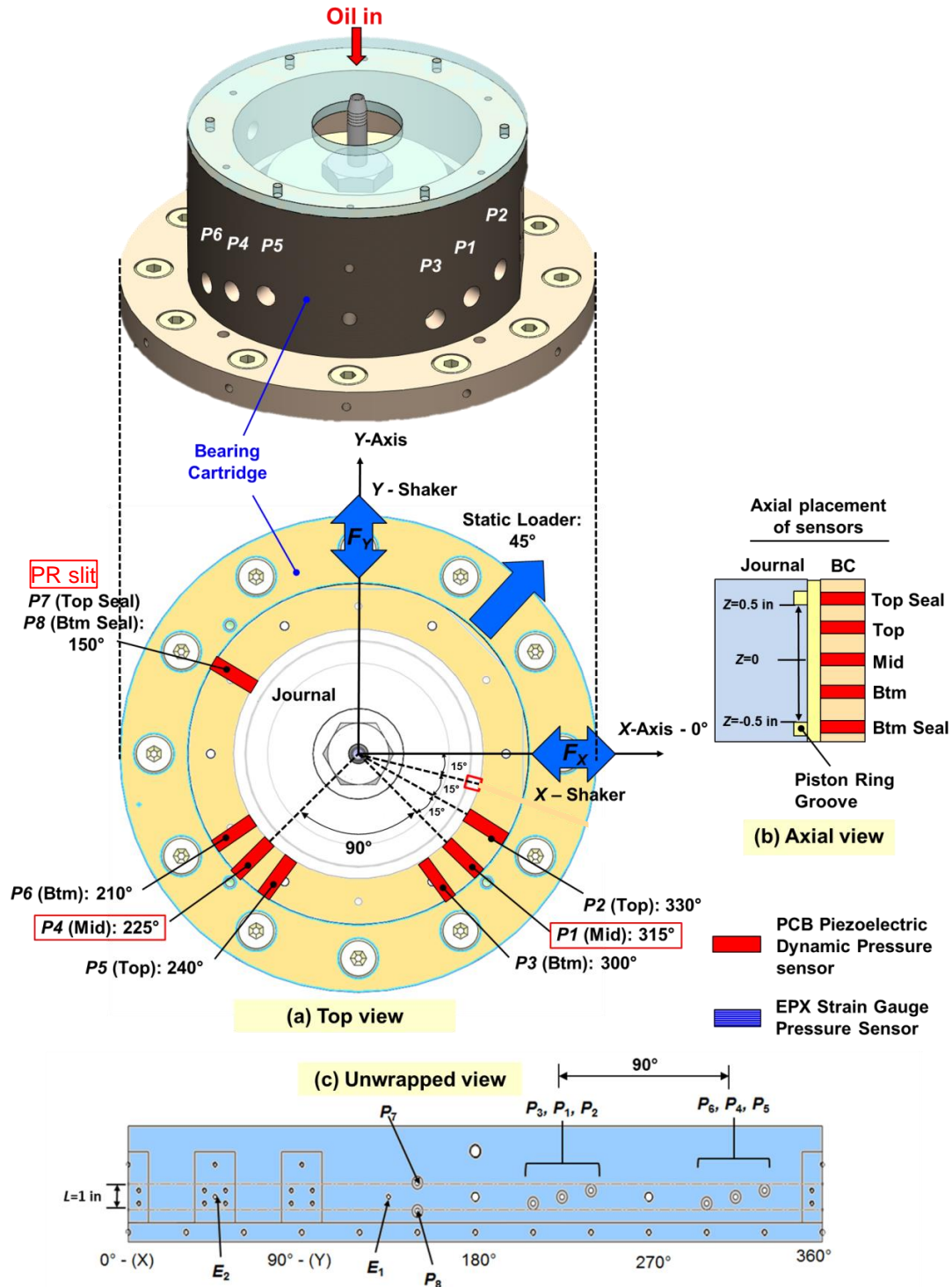
Figure 11. Schematic views of the disposition of pressure sensors in the BC: (a) top view, (b) axial view and (c) unwrapped view. Taken from Ref [18].

For both the piston ring and the O-ring sealed ends dampers operating with circular orbit radii (a) r/c=0.1 and (b) r/c=0.3, Figure 12 and Figure 13 depict the measured *peak-to-peak* film dynamic pressure at the mid-plane (z=0) and θ=225° versus whirl frequency. The lubricant supplies through a feedhole at θ=45° at z=0 with supply pressure (P_s) at 0.7, 3.5, and 6.2 bar.

The *peak-to-peak* film dynamic pressure linearly increases with an increase in whirl frequency. For a small squeeze film velocity ($V_s=r\omega<0.014$ m/s), the *peak-to-peak* dynamic pressures stay relatively constant under various P_s. For a large squeeze film velocity ($V_s=r\omega>0.014$ m/s), the *peak-to-peak* film dynamic pressure raises as P_s increases.

For both sealed ends dampers operating with at a low lubricant supply pressure (P_s=0.7 bar), the *peak-to-peak* pressure for orbit radius r/c=0.3 increases with an increase in frequency for the low frequency range (ω<60 Hz). For a higher frequency (ω>60 Hz), the *peak-to-peak* pressure reaches an asymptote as marked by a red dashed ellipse on the graph. Note the asymptote line at ½($P_{p\text{-}p}$) ~P_a ~1 bar evidences air ingestion. The PR sealed ends damper *peak-to-peak* pressure reaches the asymptote at a lower frequency than the O-ring sealed ends SFD does.

For a motion with whirl radius (r/c=0.3) and with a low P_s=0.7 bar, the lubricant supplied thru the feedhole is not enough to fill the film gap. As a result, air enters the fluid film when the film pressure is below P_a. Further evidence follows when depicting some pressure profiles.

For two orbit radii, r/c=0.1 and 0.3, Figure 14 displays the *peak-to-peak* dynamic film pressure recorded at the mid-plane (z=0) and θ=225° versus whirl frequency for operation with PR seals and O-ring seals. P_s=0.7, 2.1 and 6.2 bar. Clearly, the *peak-to-peak* dynamic pressure increases with an increase in orbit amplitude. The dynamic pressure for an orbit radius r/c=0.3 (with supply pressure of 2.1 and 6.2 bar) is ~ thrice that recorded in tests with r/c=0.1. However, for r/c=0.3 and P_s=0.7 bar, the *peak-to-peak* film dynamic pressure reaches ~2 bar and remains constant as the whirl frequency increases. This observation evidences lubricant vapor cavitation and/or air ingestion.
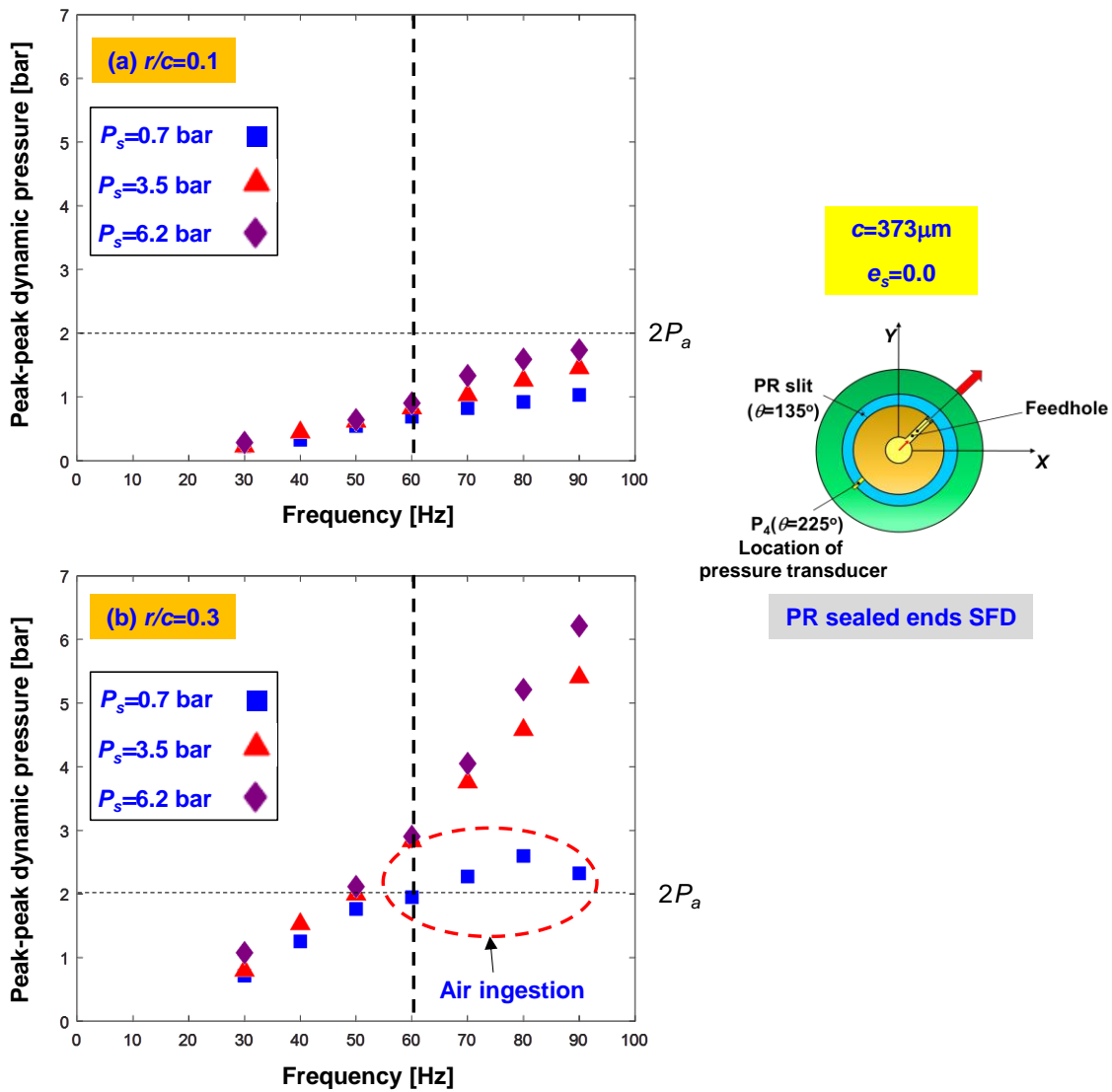
Figure 12. Recorded *peak-to-peak* film dynamic pressure ($z=0$, $\theta=225°$) vs. frequency for **piston ring sealed ends damper.** Lubricant supply pressure P_s=2.1 bar, 3.5 bar and 6.2 bar. Centered circular orbit tests with radius (a) r/c=0.1 and (b) r/c=0.3.
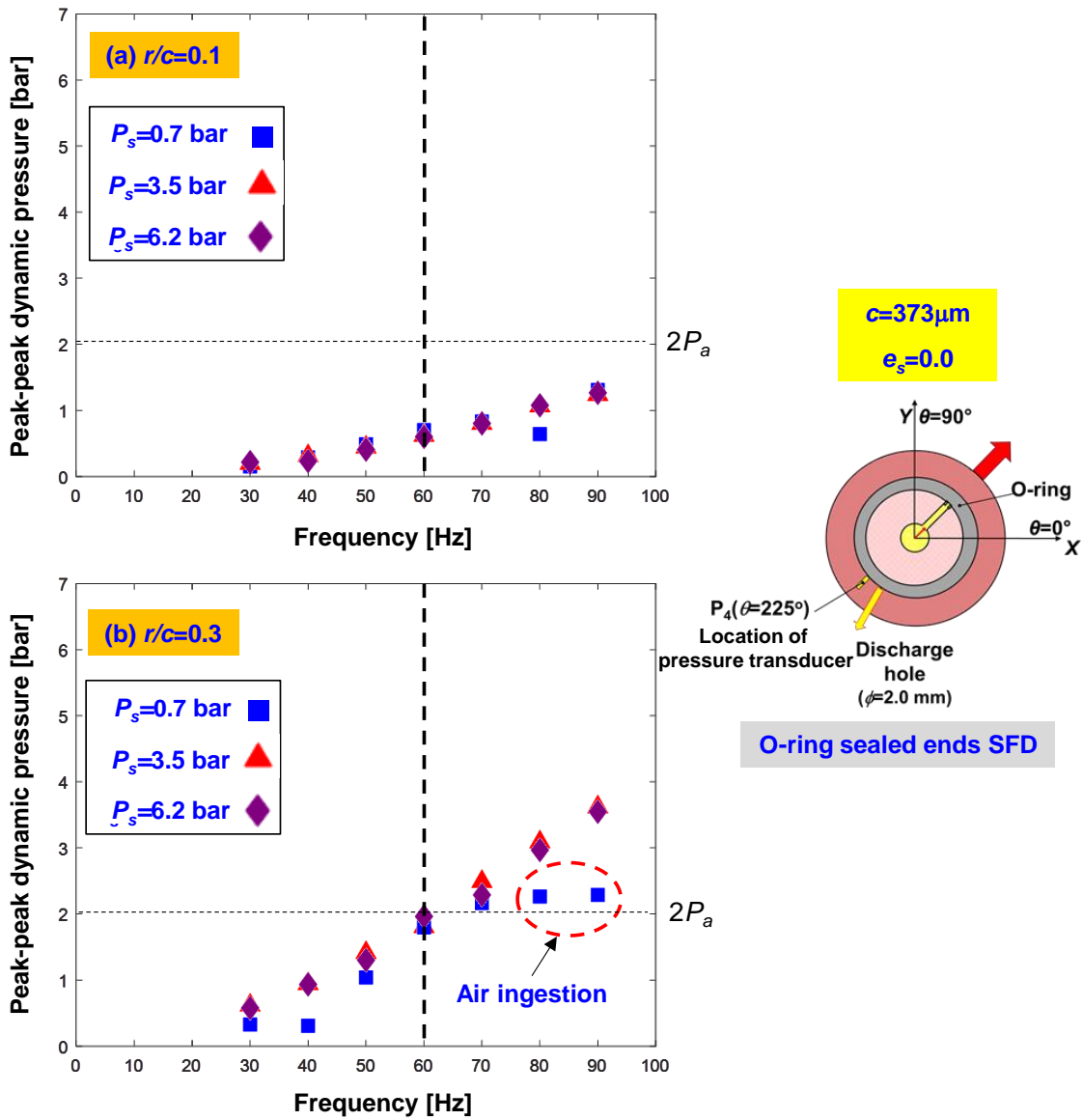
Figure 13. Recorded *peak-to-peak* film dynamic pressure (z=0, θ=225º) vs. frequency for an O-ring sealed ends damper. Lubricant supply pressure P_s=2.1 bar, 3.5 bar and 6.2 bar. Centered circular orbit tests with radius (a) r/c=0.1 and (b) r/c=0.3.
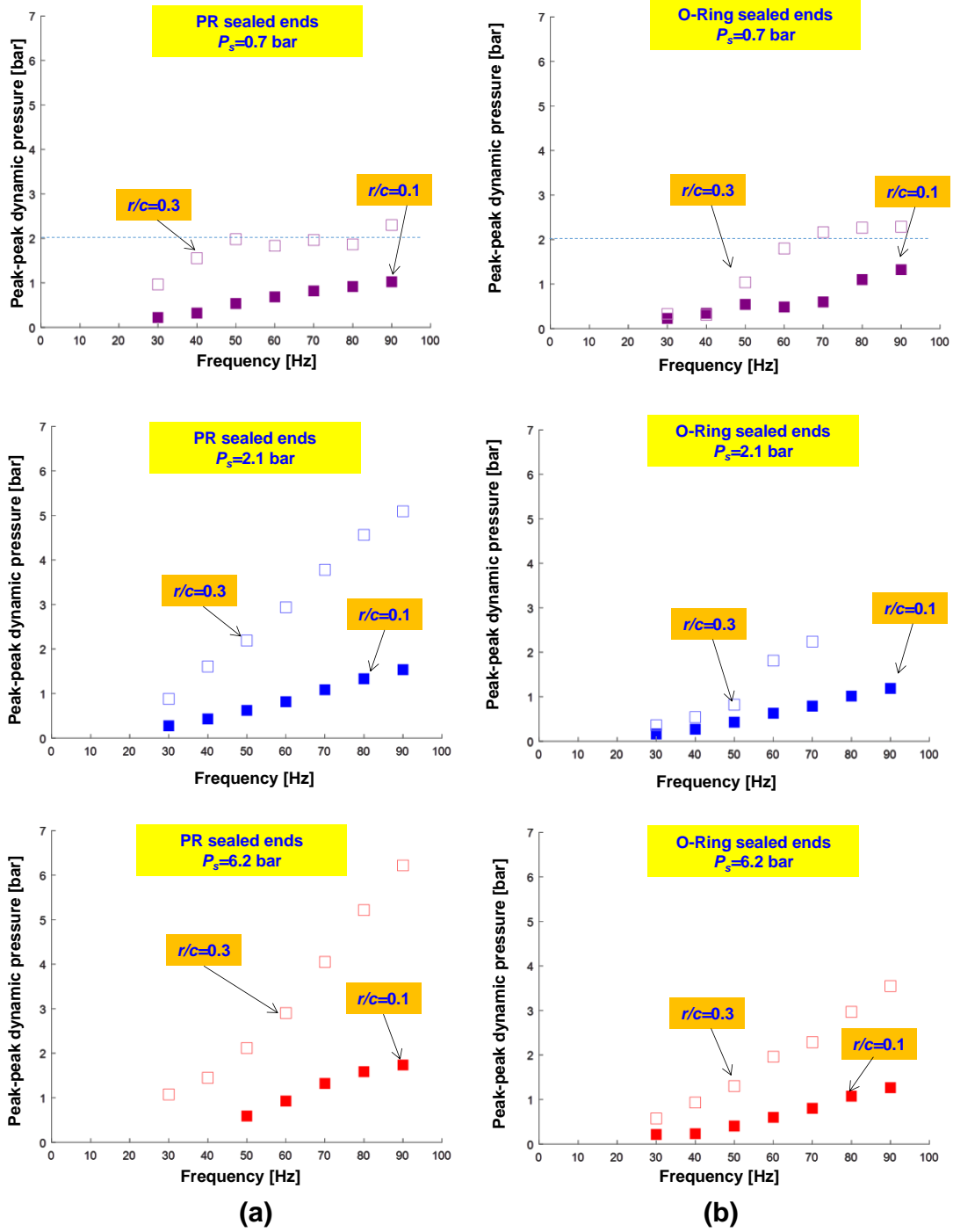
Figure 14. Recorded *peak-to-peak* film dynamic pressure ($z=0$, $\theta=225°$) vs. whirl frequency for (a) PR sealed ends SFD and (b) O-ring Sealed ends SFD. Circular centered orbits with radii $r/c=0.1$ and $r/c=0.3$ ($e_s=0$). Operation with lubricant supply pressure $P_s=$ 0.7, 2.1, and 6.2 bar thru one feedhole.

Examples of Recorded Squeeze Film Dynamic Pressures Profiles[6]

For the PR sealed ends damper supplied with pressure P_s of (a) 0.7 bar (b) 2.1 bar (c) 3.5 bar, (d) 6.2 bar at a whirl frequency ω=90 Hz, Figure 15 and Figure 16 show recorded pressure data and film thickness for whirl radii r/c=0.1 and r/c=0.3. Note that the scale for dynamic pressure in Figure 15, from -2.0 to 2.0 bar, is smaller than the scale shown in Figure 16. The figures display three periods of whirl motion (T=11 ms) recorded at mid-plane z=0 and θ=225°. The film thickness at θ=225° is

$$h_{(\Theta,t)} = c + X_{(t)} \cos\theta + Y_{(t)} \sin\theta \tag{7}$$

$$X_{(t)} = r\cos(\omega t + \phi_X) \tag{8a}$$

$$Y_{(t)} = r\cos(\omega t + \phi_Y) \tag{8b}$$

where r is the orbit radius; ϕ_X and ϕ_Y are the arguments of the fundamental components of the Fourier series built functions from the measured displacements along the X, Y axes.

In Figure 15 and 16, the horizontal dash lines represent zero absolute pressure. Note that the position of the zero absolute pressure line is different in each graph since the Y-axis scale on the right side is a dynamic pressure. The total pressure is the sum of dynamic pressure and static pressure, i.e., $P_{total}=P_{Dynamic}+P_{Static}$. The magnitude of the dynamic pressure increases with an increase in orbit amplitude.

For r/c=0.1, the pressure profiles for operations with P_s=2.1, 3.5, 6.2 bar are almost identical, whereas the pressure profile for a supply pressure P_s=0.7 bar shows a much lower peak-to-peak pressure and a flat (constant) pressure zone at the maximum film thickness location. Note that the pressure profiles show a distinct spike when the film thickness is decreasing. The spike may be due to the large leakage thru the PR slits, as spikes are not recorded with the O-ring sealed ends SFD.

For r/c=0.3, the film dynamic pressure profiles with a large supply pressure (P_s=3.5 bar and 6.2 bar) are almost the same, whereas the pressure profiles with a small supply pressure (P_s=0.7 bar and 2.1 bar) show smaller peak-to-peak pressures. Note the pressure profile with P_s=2.1 bar shows small pressure fluctuations, which seems to be related to fluid compressibility (mixture of air and oil) [19,20].

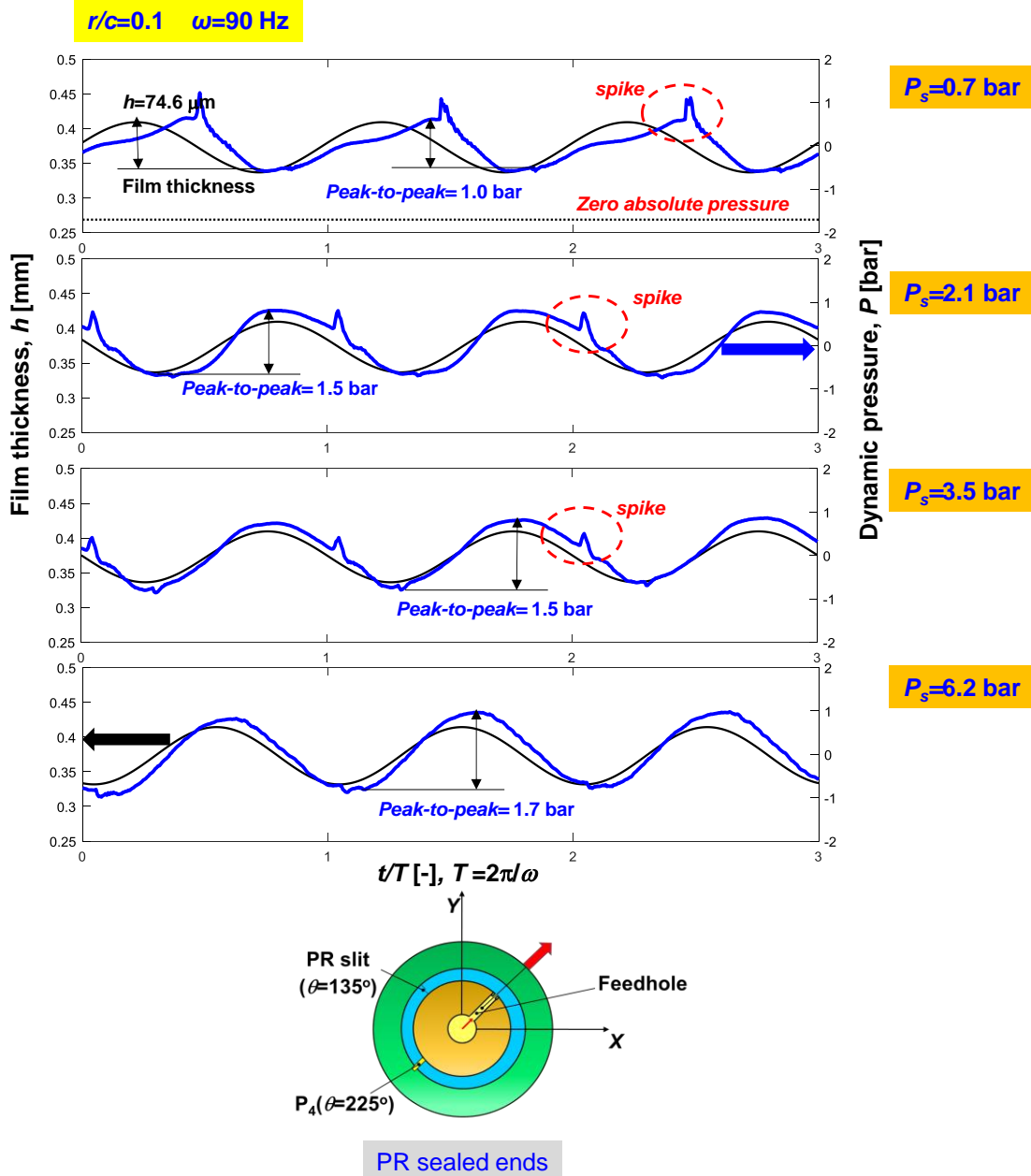[6] Portions of this section reproduce ad-verbatim information presented in Ref.[18].

Figure 15. Dynamic film pressure and film thickness recorded at mid-plane (z=0 and θ=225°) and vs. time. **PR sealed ends damper** (c=373 μm) with oil inlet pressure P_s= (a) 0.7 (b) 2.1 (c) 3.5 and (d) 6.2 bar. Circular orbit with frequency ω=90 Hz and r/c=0.1.
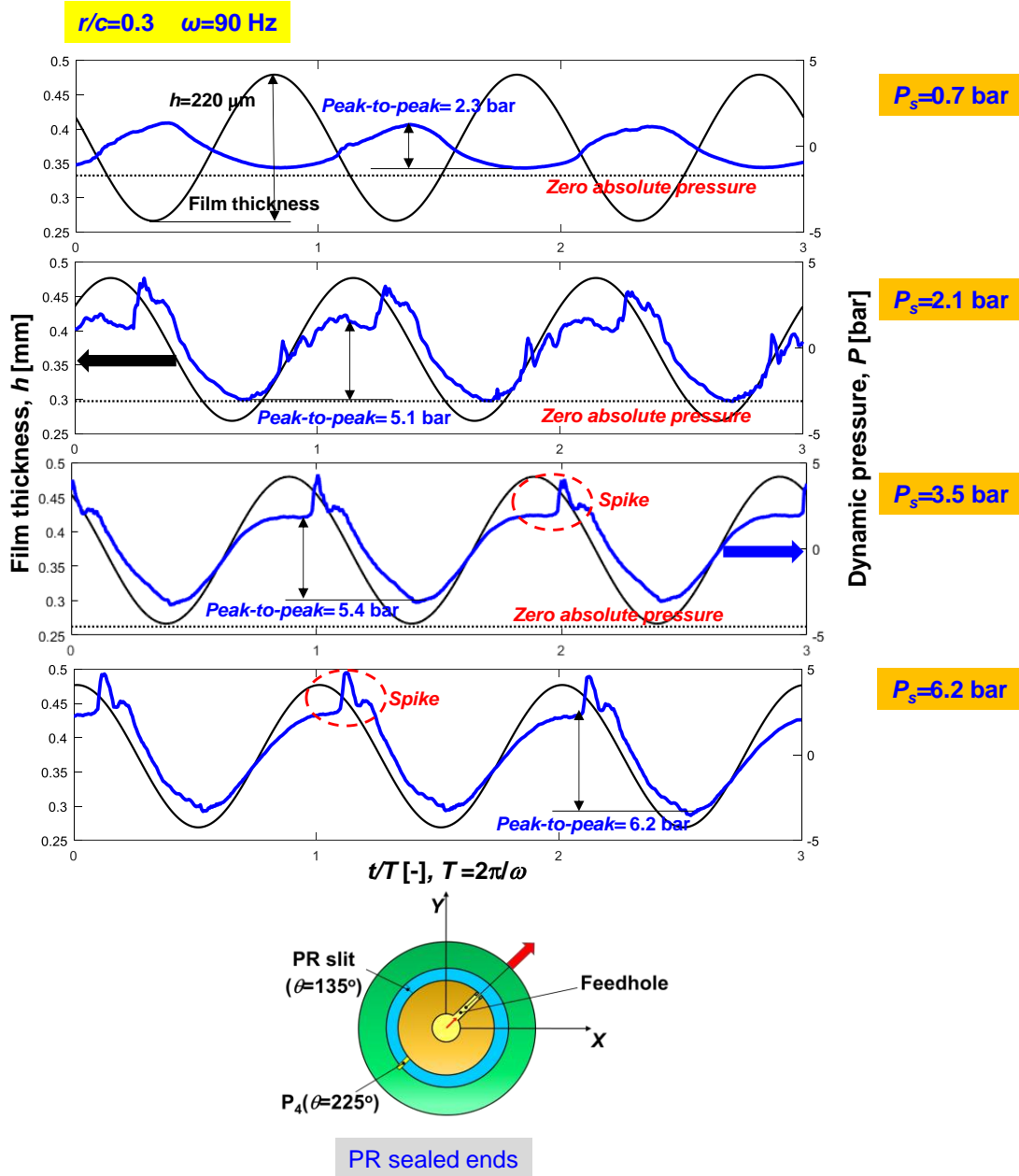
Figure 16. Dynamic film pressure and film thickness recorded at mid-plane (z=0, θ =225º) vs. time. PR sealed ends damper (c=373 μm) with oil inlet pressure P_s= (a) 0.7 (b) 2.1 (c) 3.5 and (d) 6.2 bar. Circular orbit with frequency ω=90 Hz and r/c=0.3.

Figure 17 and

Figure 18 show the film thickness and dynamic pressure profiles for the O-ring sealed ends damper operating with P_s ranging from 0.7 bar to 6.2 bar. The tests are for orbits with radii r/c=0.1 and r/c=0.3, and whirl frequency ω=90 Hz. Note that scale for dynamic pressure in

Figure 17 is set to -2.0 to 2.0 bar.

In Figs. 17 and 18, none of the dynamic pressure profile reaches zero absolute pressure. For operations with a small supply pressure ($P_s < 3.5$ bar for r/c=0.1 and $P_s < 3.5$ bar for r/c=0.3), the film *peak-to-peak* dynamic pressure decreases as the supply pressure (P_s) decreases, whereas there is not noticeable change in *peak-to-peak* pressure for operation with a large supply pressure. For operation with a low supply pressure and with a high squeeze film velocity (V_s), the dynamic pressure profile shows a flat (constant) pressure zone ($\sim P_a$), see Fig. 18(a)
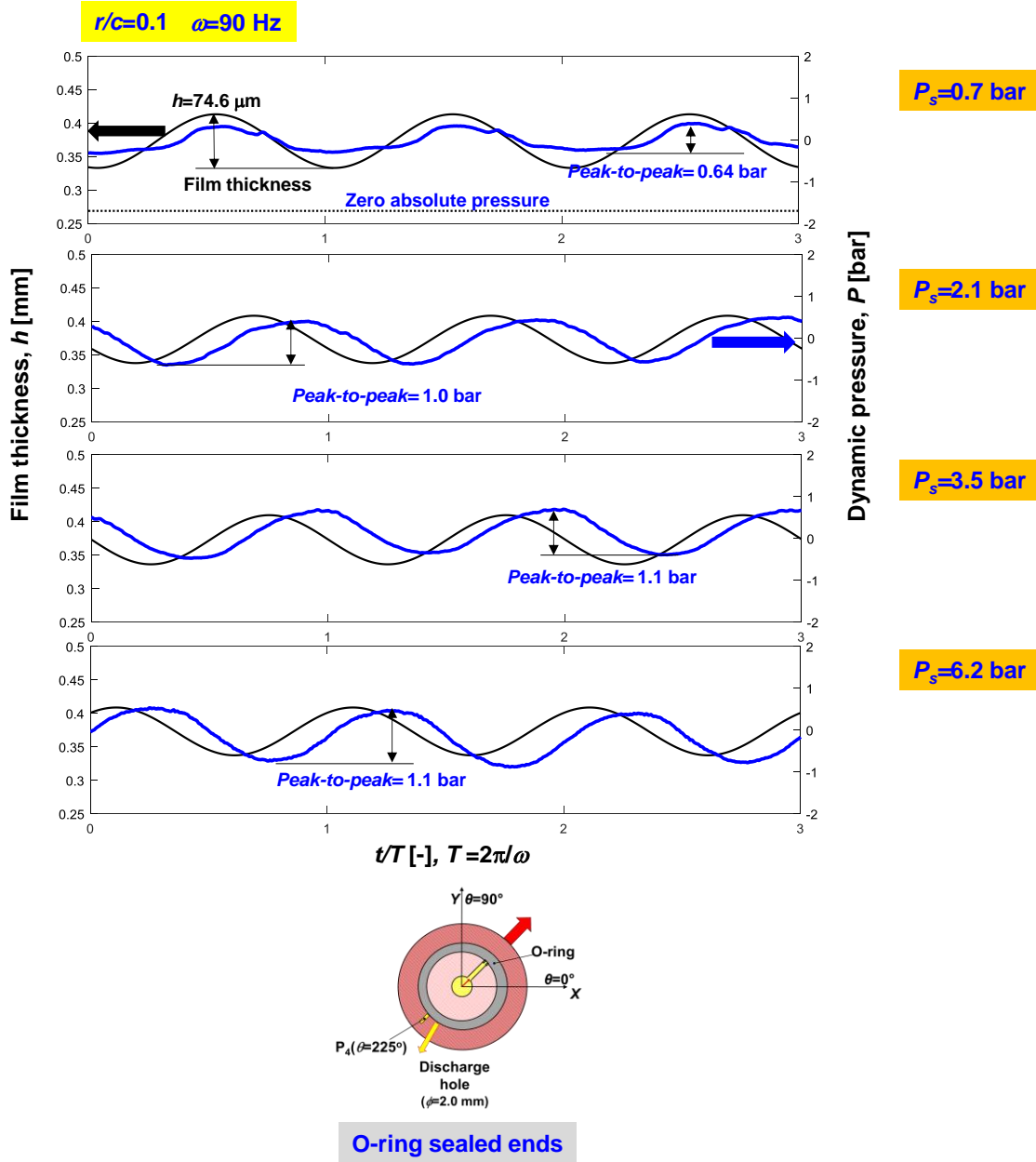
Figure 17. Dynamic film pressure and film thickness recorded at mid-plane and θ=225° vs. time. O-ring sealed ends damper (c=373 μm) with oil inlet pressure P_s= (a) 0.7 (b) 2.1 (c) 3.5 and (d) 6.2 bar. Circular orbit with frequency ω=90 Hz and r/c=0.1.

Figure 18. Dynamic film pressure and film thickness recorded at mid-plane and θ=225° vs. time. O-ring sealed ends damper (c=373 μm) with oil inlet pressure P_s= (a) 0.7 (b) 2.1 (c) 3.5 and (d) 6.2 bar. Circular orbit with frequency ω=90 Hz and r/c=0.3.

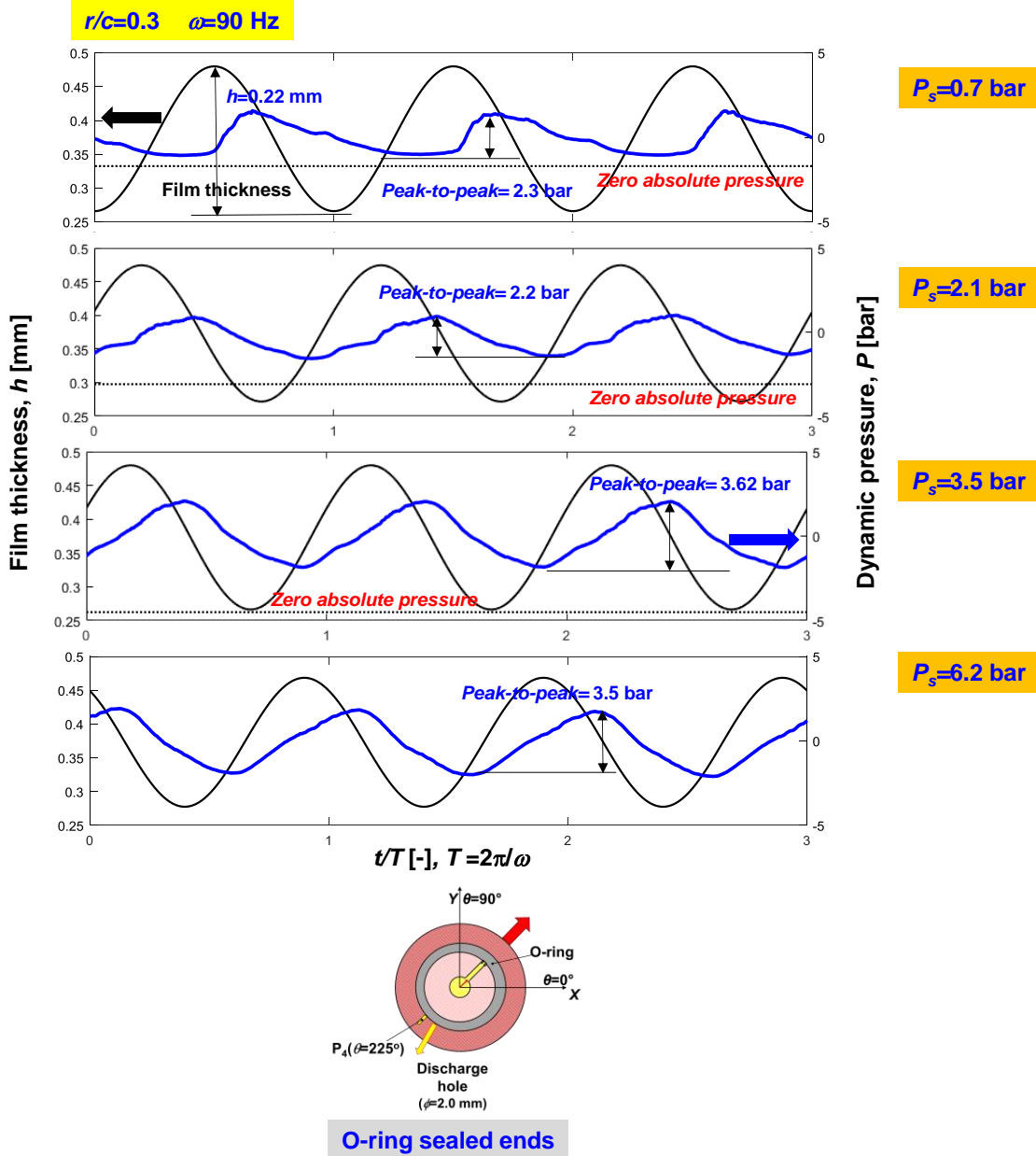# Conclusions

The reports consolidates measurements of the dynamic forced response of a short length SFD (L/D=0.2) sealed with either piston rings (PRs) or with O-ring. In the tests with ISO VG 2 lubricant, the supply pressure through one feed hole varies from P_s=0.7 bar(g) to 6.2 bar (g). Exerted single frequency loads produce circular centered orbits with radii r=0.1c and 0.3c. The parameter identification delivers force coefficients valid over a frequency range (10 Hz-100 Hz). The major conclusions drawn are:

a. For a large supply pressure (P_s>~2.1 bar) and flow rate (Q_s~2.1 LPM for PR sealed ends SFD, 3.2 LPM for O-ring sealed ends SFD), the damping coefficient C_{avg} ~ 11 kN-s/m) does not change with an increase in orbit radius (r/c from 0.1 to 0.3). Added mass coefficient (M_{avg}) are nearly constant at ~30 kg.

b. For a small squeeze film velocity (V_s=$r\omega$< 0.014 m/s), film *peak-to-peak* dynamic pressures stay relatively constant for operation with an increase in P_s. For V_s= $r\omega$> 0.014 m/s, the film *peak-to-peak* dynamic pressure increases as P_s increases.

c. Operation with a low supply pressure causes a reduction in film dynamic pressures and introduces air ingestion into the film land.

d. In separate tests where the lubricant flow into the damper is cut, the amplitude of whirl motion drastically increases. The effect of a lubricant loss on the SFD test rig response is more significant when the initial supply flow Q_s (or supply pressure P_s) is large. The magnitude of the journal whirl motion for the O-ring sealed ends damper is smaller than the one for the PR sealed ends damper due to the stiffness and damping from the O-ring material.

References

[1] San Andrés, L., 2012, *Modern Lubrication Theory*, "Squeeze Film Dampers (SFDs)," Notes 13, Texas A&M University Digital Libraries, http://oaktrust.library.tamu.edu/handle/1969.1/93197 [May 19th, 2017].

[2] Vance, J., Zeidan, F., and Murphy, B., 2010, *Machinery Vibration and Rotordynamics*, John Wile & Sons, New York, Inc, 2010, pp. 216-238.

[3] Zeidan, F., and Vance, J., 1990, "Cavitation and Air Entrainment Effects on the Response of Squeeze Film Supported Rotors," ASME J. Tribol.*,* **112**, 347-353.

[4] Vance, J., and Kirton, A.,1974, "Preliminary Investigation of the Dynamic Force Response Coefficients for Squeeze Film Bearing Dampers," University of Florida, Gainesville.

[5] Feder, E., Bansal, P. N., and Blanco, A., 1978, "Investigation of Squeeze Film Damper Forces produced by Circular Centered Orbits," ASME J. Engineering for Power, **100**, 15-21

[6] Bansal, P. N., and Hibner, D. H., 1978, "Experimental and Analytical Investigation of Squeeze Film Bearing Damper Forces induced by Offset Circular Whirl Orbits," ASME J. Mechanical Design, **100**, 549-557

[7] Marmol, R., and Vance, J., 1978, "Squeeze Film Damper Characteristics for Gas Turbine Engines," ASME JMD., **100**, 139-146.

[8] Miyachi T., Hoshiya S., Sofue Y., Matsuki M., and Torisaki T., 1979, "Oil Squeeze Film Dampers for Reducing Vibration of Aircraft Gas Turbine Engines". ASME. Turbo Expo: Power for Land, Sea, and Air, Paper No. 79-GT-133.

[9] Lund, J. W., Smalley, A. J., Tecza, J.A., and Walton, J. F., 1983, "Squeeze Film Damper Technology: Part 1-Prediction of Finitie Length Damper Performance," *Proc. of ASME 1983 International Gas Turbine Conference and Exhibit*, Pheonix, AZ, March, 1983.

[10] San Andrés, L., and Vance, J. M., 1987, "Effects of Fluid Inertia on Finite-Length Squeeze Film Dampers," ASLE Trans., **30**(3), 384-393.

[11] Jung, S. Y., and Vance, J. M., 1993, "Effects of Vapor Cavitation and Fluid Inertia on the Force Coefficients of a Squeeze Film Damper Part I-Analysis of a Long SFD," Trib. Trans., **36**, 597-604.

[12] Kim, K.-J., and Lee, C.-W, 2005, "Dynamic Characteristics of Sealed Squeeze Film Damper With a Central Feeding Groove," J. Trib., **127**, 103-111.

[13] Levesley, M. C., and Holmes R., 1996, "The Effect of Oil Supply and Sealing Arrangements on the Performance of Squeeze-Film Dampers: an Experimental Study," Journal of Engineering Tribology, **210**, pp. 221-232.

[14] Arauz, G. L,, and San Andrés, L. A., 1996, "Experimental Study on the Effect of a Circumferential Feeding Groove on the Dynamic Force Response of a Sealed Squeeze Film Damper," ASME J. Tribology, **118**, pp. 900-905

[15] De Santiago, O. C., San Andrés, L., 1999, "Imbalance Response and Damping Force Coefficientsof a Rotor Supported on End Sealed Integral Squeeze Film Dampers," *International Gas Turbine & Aeroengine Congress & Exhibition*, Indianapolis.

[16] Della Pietra L. and Adiletta, 2002, "The Squeeze Film Damper over Four Decades of Investigations. Part I: Characteristics and Operating Features," The Shocl and Vibration Digest, **34**(1), pp. 3-26.

[17] San Andrés, L., and Seshagiri, S., 2013, "Damping and Inertia Coefficients for Two End Sealed Squeeze Film Dampers With a Central Groove: Measurements and Predictions," ASME J Gas Turb Pwr, **135**(11).

[18] Jeung, S.-H., and San Andrés, L., 2016, "Experimental Response of an Open Ends SFD Versus a Sealed Ends SFD," Research Progress Report to the TAMU Turbomachinery Research Consortium (TRC), TRC-SFD-01-2016, Texas A&M University, College Station, TX, May.

[19] Zeidan, F., and Vance, J., 1989, "Cavitation Leading to a Two Phase Fluid in a Squeeze Film Damper," Triobol. Trans., **32**(1), pp. 100-104.

[20] San Andrés, L., and Diaz, S., 1998, "Measurements of Pressure in a Squeeze Film Damper with an Air/Oil Bubbly Mixture," Tribol. Trans, **41**(2), pp. 282-288

Appendix A. Measurement of Lubricant Physical Properties

The lubricant used during testing is ISO VG 2 grade oil. A Brookfield DV-E rotary viscometer was used to measure the viscosity of the lubricant. The apparatus measures the fluid viscosity at given shear rates with a rotating spindle that is submerged in the fluids. The viscous drag of the fluid against the spinning motion of the spindle is measured by the deflection of a calibrated spring. A water jacket heat the container with the lubricant. The ASTM viscosity-temperature relationship is

$$\mu = \mu_R e^{-\alpha_v(T-T_R)}$$
(B.1)

where $\mu_R = 2.57$ *mPas* is the measured viscosity at room temperature ($T_R = 27$°C). The oil viscosity coefficient, α_v, is given as

$$\alpha_v = \frac{-\ln(\mu_2/\mu_R)}{(T_2-T_R)} = 0.0199 \frac{1}{°C}$$
(B.2)

where μ_2 and T_2 are the previous viscosity and temperature values, respectively.

From numerous tests performed during years of research program, some of lubricant leak thru pipes, valves or oil tank, and so a new lubricant (19 liter) is purchased and refilled into the oil tank. Figure A.1 shows the measured viscosity of the new, used lubricants, and mixture of the two. The plot also includes the ASTM standard curve fit. The viscosity measurements of the used and new lubricant show similar results, indicating no significant changes in lubricant properties have occurred.

Note that the manufacturer's specification for viscosity at 40 °C is 2.1 mPa-s while the measurement indicates that the viscosity at the same temperature is 2.008 mPa-s. The discrepancy is most likely due to dissolved air from repeated testing.

At ambient condition of 27 °C, the lubricant density was determined by measuring the weight a known volume of lubricant oil. The oil density obtained is $\rho=820$ kg/m^3.
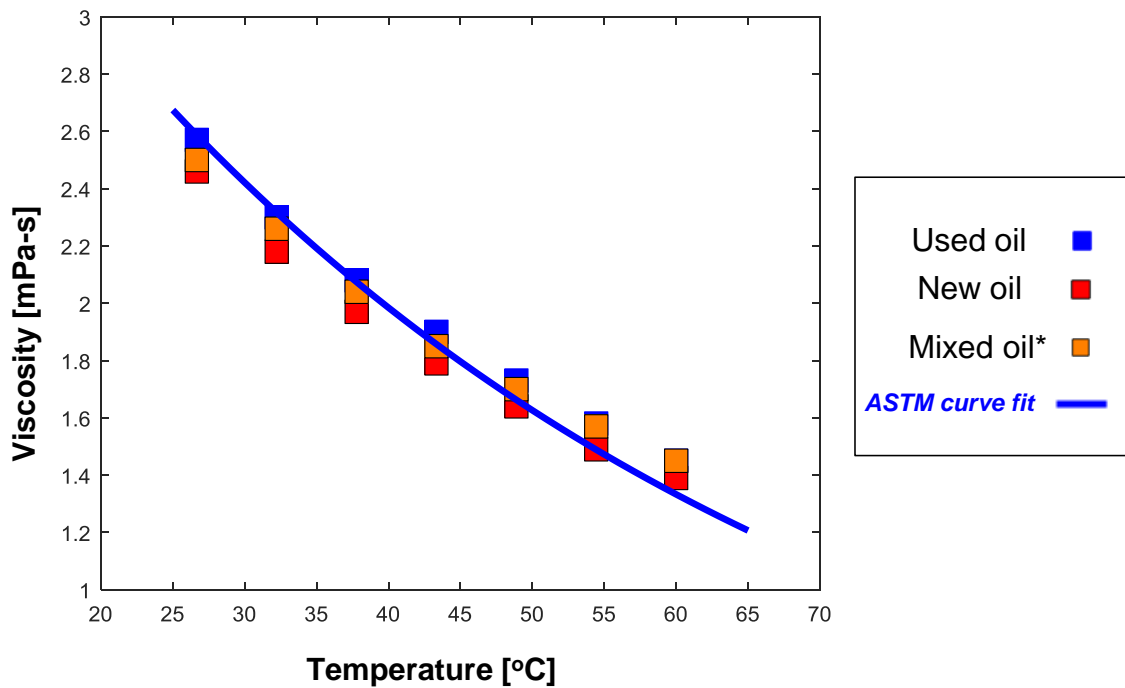
*New oil (5 liter) poured into a tank filled with used oil (March 2017).

Figure A.1. ISO VG 2 measured viscosity versus temperature for three separate measurements.

Table A.1. Mobil Velocite™ No 3 (ISO VG 2) Manufacturer specification [A1]

Mobil Velocite Oil Numbered Series No 3 (ISO VG 2)	
cSt @ 40ºC	2.1
cSt @ 100ºC	0.95
Pour Point, ºC	-36
Flash Point, ºC	84
Density @ 15º C, kg/L	0.802

References

[A1] "Mobil Velocite™ No 3 (ISO VG 2) Manufacturer specification sheet", Hydraulic oils Typical Properties, Mobil, Accessed October 2013, http://www.mobil.com/USAEnglish/Lubes/PDS/GLXXENINDMOMobil_Velocite _Oil_Numbered.aspx

Appendix B. Identification of (Dry) Test System Structure Parameters[7]

Circular orbit load tests are performed with a dry system (without lubricant) to identify the test system structural parameters [structural stiffness (K_s), system remnant mass (M_s), and structural damping (C_s)]. Two electromagnetic shakers deliver single frequency loads, 90º out of phase, over a designated frequency range of 10–90 Hz. The amplitude of journal motion is set to r/c=0.1.

The Instrumental Variable Filter (IVF) method [18] estimates the force coefficients for the dry system (K_S, C_S, M_S) from the complex dynamic stiffness

$$[H_S]_{XX,YY} = [K_S - \omega^2 M_S + i\omega C_S]_{XX,YY}$$

where ω is the excitation frequency. Note

$$\text{Re}(H_S) \rightarrow K_S\text{-}\omega^2 M_S \text{ and } \text{Im}(H_S) \rightarrow \omega C_S$$

reveal the structural stiffness (K_S) and system remnant mass (M_S) and an (assumed) viscous damping coefficient (C_S).

Figure B1 shows the experimental data and physical model fits for both open ends and O-ring sealed conditions. The correlation for the imaginary part of H are low (R^2 <<1), indicating the structural damping (C_S) is not of viscous type. $R^2 > 0.9$ for $\text{Re}(H)$ indicating that the model presents accurately the structure.

Table B1 lists the identified test system structural parameters (K_S, C_S, M_S) valid over a frequency range, ω=10-250 Hz. The results show that the test system is orthotropic $(K_{XX}>K_{YY})_S$ with little structural cross-coupling. The average structure stiffness is K_s=1.6 MN/m.

Table B2 lists the identified test system structural parameters (K_S, C_S, M_S) with the O-rings installed. The excitation frequency range is ω=10-250 Hz. With O-rings installed, the structural stiffness $K_{S+O\text{-}ring} \sim K_S$+0.6 MN/m and $C_{S+O\text{-}ring} \sim C_S$ + 0.7 kN-s/m. That is, the O-rings provide (substantial) stiffness and damping coefficients. The O-ring stiffness is ~20% of the total (dry) system stiffness.

---

[7] Portion of this section reproduce ad verbatim information presented in [18]
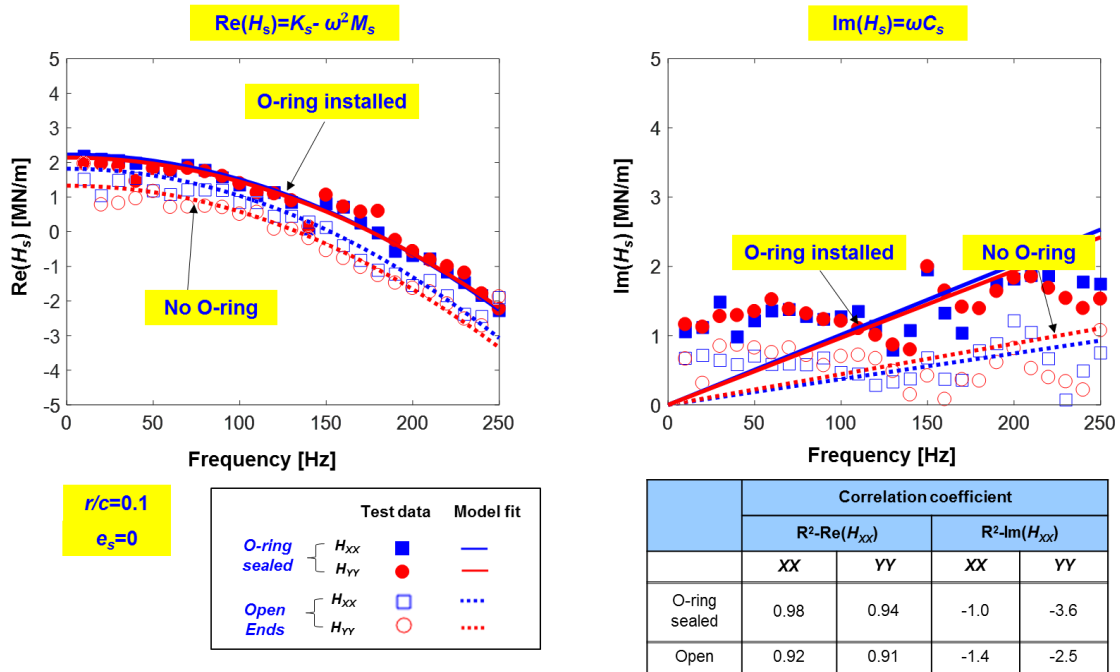
Figure B1. Dry test (without lubricant) system: Real and imaginary parts of system direct complex stiffness versus excitation frequency. Centered circular orbit dynamic load tests. Orbit amplitude *r/c*=0.1 for O-ring sealed and open ends. Test frequency range is 10 Hz to 250 Hz. Nominal radial clearance is *c*=0.373 mm.

Based on the free-response of an underdamped ($\zeta<1$) one degree of freedom mechanical system, $\zeta = \dfrac{C}{2\sqrt{K_S M}}$ is the damping ratio and $\omega_n = \sqrt{\dfrac{K_S}{M}}$ is the system natural frequency. Above, $M = M_{BC} + M_S$, where M_{BC}=15 kg and M_{SFD} is the SFD added mass, and $K_S = 1.6$ MN/m is the support structural stiffness.

Table B1. Open ends SFD system structural parameters obtained from circular orbit tests under a dry condition (no lubricant). Parameters identified in frequency range 10 – 250 Hz. Orbit amplitude *r/c*=0.1 and static eccentricity *e$_s$/c*=0.0.

Structural parameter			Direct		Cross-coupled	
			XX	*YY*	*XY*	*YX*
Stiffness	K_S	[MN/m]	1.8	1.3	0.4	0.1
Damping	C_S	[kN.s/m]	0.6	0.7	-0.2	-0.2
Mass	M_S	[kg]	1.9	1.9	0.4	0.2
System Mass	M_{BC}	[kg]	15.2			
Natural Frequency	ω_n	[Hz]	55	47		
Damping Ratio	ζ_n		0.06	0.08		

Table B2. O-ring sealed ends SFD system structural parameters obtained from circular orbit tests under a dry condition (no lubricant). Parameters identified in frequency range 10 – 250 Hz. Orbit amplitude *r/c*=0.1 and static eccentricity *e$_s$/c*=0.0.

Structural parameter			Direct		Cross-coupled	
			XX	*YY*	*XY*	*YX*
Stiffness	$K_{S+O\text{-}ring}$	[MN/m]	2.2	2.1	-0.3	0.1
Damping	$C_{S+O\text{-}ring}$	[kN.s/m]	1.6	1.5	-0.1	0.04
Mass	$M_{S+O\text{-}ring}$	[kg]	1.8	1.8	-0.3	0.7
O-ring stiffness	$K_{O\text{-}ring}$	[MN/m]	0.4	0.8	-0.7	0.0
O-ring damping	$C_{O\text{-}ring}$	[kN.s/m]	1.0	0.8	0.1	0.2
System Mass	M_{BC}	[kg]	15.2			
Natural Frequency	ω_n	[Hz]	61	60		
Damping Ratio	ζ_n		0.14	0.14		

Appendix C. Uncertainty in Identified Force Coefficients[8]

This section outlines the calculation of uncertainties in the identification of SFD force coefficients. The total uncertainty consists of bias uncertainty and precision uncertainty. Procedure for obtaining each uncertainty is described in detail below with B, P, and U denoting bias, precision and total uncertainty respectively. The following outline also includes a sample calculation for each type of uncertainty with a specific operating condition.

Bias uncertainty

Bias uncertainty, also known as systematic error, is most due to sensor resolution and DAQ board.

- The data acquisition (NI cDAQ-9172) system uses NI 9215 analog input module to record voltage from the sensors. The NI 9215 module has ±10V operating voltage range and 16 bits resolution [C1]. As a result, the best resolution is one part of 2^{16} or 0.00153% of the full scale, which corresponds to 0.31 mV.

- The DAQ board samples at a rate of 16,384 samples/sec and stores 4096 samples, resulting in an uncertainty of 1 Hz in the output frequency. This corresponds to $B_\omega = 10\%$ at the lowest testing frequency of 10 Hz, $B_\omega = 0.5\%$ at the highest testing frequency of 200 Hz and $B_\omega = 1.8\%$ across the entire testing frequency range.

- The X and Y REBAM (displacement) sensors has sensitivity of X=33.5 V/μm and Y=35.0 V/μm, respectively. The DAQ board records sensor voltages to a resolution of 0.31 mV, giving an uncertainty value of 9.1×10^{-3} μm. Since the largest uncertainty occurs at the smallest whirl amplitude (r/c=0.05, r=18.7 μm), uncertainty in the displacement measurement gives

$$B_{disp} = \frac{9.1 \times 10^{-3}}{18.7} \times 100\% = 0.049\% .$$

- The PCB load cells have sensitivity that is 2.2 mv/N. The DAQ precision renders an uncertainty of 0.14 N. Since the smallest recorded dynamic load at r/c=0.05 is 159 N. the uncertainty in the load measurement is

---

[8] This section reproduce ad verbatim information presented in [18].

$$B_{load} = \frac{0.14}{159} \times 100\% = 0.089\%$$

- The PCB accelerometer with sensitivity 100 mV/g, along with the DAQ uncertainty, gives uncertainty that is 0.0031 g. The smallest recorded acceleration recorded at r/c=0.05 and low frequency is 0.8541 g. As a result, the resulting uncertainty in the acceleration measurement is

$$B_{accel} = \frac{0.0031}{0.8541} \times 100\% = 0.36\%$$

With the individual bias uncertainties, the total propagation of uncertainty can be calculated using Kline-McClintock method [C3]. Using knowledge about frequency domain relations $K \sim \frac{F - M_{BC} \times a}{D}, C \sim (\frac{F - M_{BC} \times a}{D})\omega, M \sim (\frac{F - M_{BC} \times a}{D})\omega^2$, the total bias uncertainty when identifying force coefficients can be determined using the following formula

$$B_K = \sqrt{B_{disp}^2 + B_{load}^2 + B_{accel}^2} = 0.37\%$$

$$B_K = \sqrt{B_{disp}^2 + B_{load}^2 + B_{accel}^2 + B_{\omega}^2} = 1.83\%$$

$$B_K = \sqrt{B_{disp}^2 + B_{load}^2 + B_{accel}^2 + 2 \times B_{\omega}^2} = 2.57\%$$

The film land force coefficients are determined by subtracting the force coefficients of the lubricated test from that of the dry test as following

$$(K, C, M)_{SFD} = (K, C, M)_L - (K, C, M)_S$$

As a result, the propagation of the bias uncertainty from the two measurements are

$$B_{K_{SFD}} = \sqrt{B_{K_S}^2 + B_{K_L}^2} = 0.5\%$$

$$B_{K_{SFD}} = \sqrt{B_{C_S}^2 + B_{C_L}^2} = 2.6\%$$

$$B_{K_{SFD}} = \sqrt{B_{M_S}^2 + B_{M_L}^2} = 3.6\%$$

Precision uncertainty

Precision uncertainty is associated with the repeatability of the experiments. A set of test with a selected range of frequencies are performed at each whirl amplitude and eccentricity. Plotting the real part of dynamic stiffness and extract the y-intercept as the stiffness coefficient K and the curvature as the inertia coefficient M. In addition, the

damping coefficient can be obtained by plotting the imaginary complex stiffness and extracting the slope of the line.

The precision uncertainty of a least square curve fit is described in the following equation [C2]

$$P = t \times S$$

t is the student's t-distribution value corresponding to the 95% confidence level [C2]. S is the precision index of the averaged result.

Relation for estimated standard deviation (S) of the intercept and slope of a least square fit line can be expressed as

$$S_{Intercept} = \sqrt{\frac{1}{N(N-2)} \frac{1-r^2}{r^2}}$$

$$S_{Slope} = \sqrt{\frac{1}{N-2} \frac{1-r^2}{r^2}}$$

N is the number of points used for curve fit and r^2 is the goodness of curve fit.

Using an example for one of the operating condition $e_s=0$, $r/c=0.1$ with $N=10$. The uncertainty of the SFD direct coefficients in the X direction are:

$$P_{K_{SFD}} = 2.9\%$$

$$P_{C_{SFD}} = 6.4\%$$

$$P_{M_{SFD}} = 9.1\%$$

Total uncertainty

The total uncertainty in each SFD force coefficients are

$$U_{K_{SFD}} = \sqrt{(B_{K_{SFD}})^2 + (P_{K_{SFD}})^2} = 2.9\%$$

$$U_{C_{SFD}} = \sqrt{(B_{C_{SFD}})^2 + (P_{C_{SFD}})^2} = 9.6\%$$

$$U_{M_{SFD}} = \sqrt{(B_{M_{SFD}})^2 + (P_{M_{SFD}})^2} = 9.8\%$$

References

[C1] "NI cDAQ – 917x User Manual," User Manual for NI CompactDAQ9171/9174/9178 USB Chassis, National Instruments, July 2011, Appendix A. Specifications.

[C2] Beckwith, T., Marangoni, R., and Lienhard, J. 1993, "Mechanical Measurements", Prentice Hall, 5th edition, pp. 82

[C3] Coleman, H.W., and Steele, G.W., 1998, *Experimentation and Uncertainty Analysis for Engineers*, John Wiley & Sons, New York.

Appendix D. Flow Measurements in Sealed Ends SFDs

Figure D1 shows the flow rate measured for both the PR and O-ring sealed ends SFD versus supply pressure. The lubricant flows thru one feedhole in the journal at $\theta=45^o$ and $z=0$. The flow rate is measured using Great Plains Industries (GPI) A1 Series flow meter, with an uncertainty of 5% [D1]. Since the flow meter shows two digits, the absolute uncertainty is ±0.04 liters. For the PR sealed ends SFD, the PR slits are located at $\theta=135^o$ and $z=\pm\frac{1}{2}L$. For the O-ring sealed ends SFD, a discharge port of diameter of 2 mm is at $\theta=225^o$ and $z=\frac{1}{4}L$. There is virtually no (side) leakage through the O-ring seals.

For the same supply pressure, the flowrate through the PR sealed ends SFD is less than half of the flowrate through the discharge hole of the O-ring sealed ends SFD.
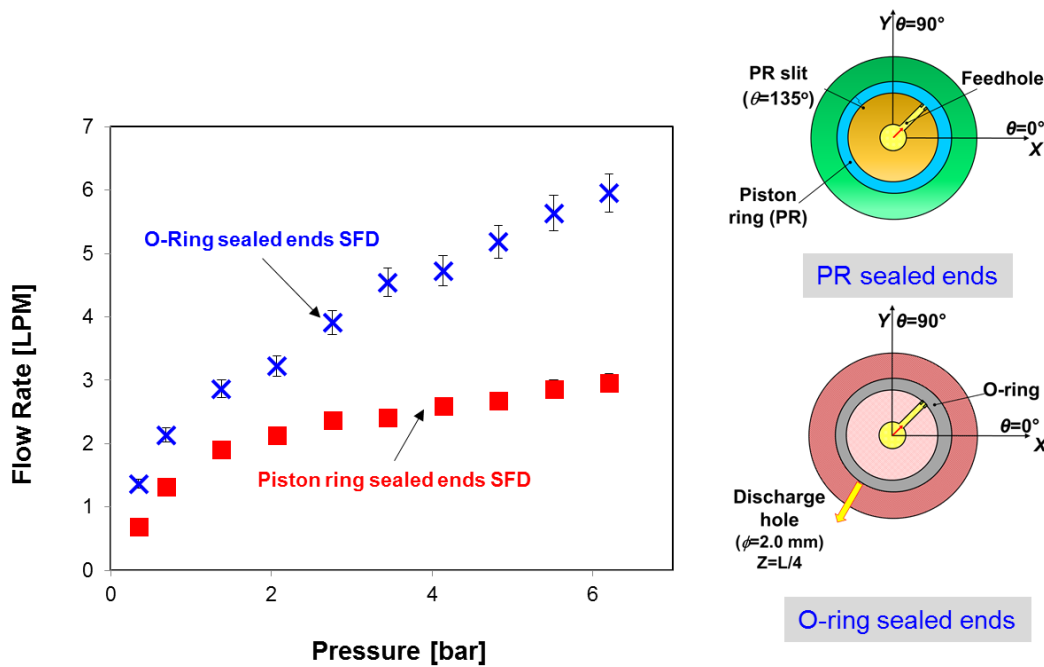
Figure D1. Lubricant flowrate (Q_s) vs. inlet supply pressure (P_s) for damper sealed with piston rings or with O-ring seals. Lubricant supplies thru a feedhole at $\theta=45^o$ at mid-plane ($z=0$). For PR sealed ends, the PR slits are at $\theta=135^o$. For the O-ring sealed ends, lubricant discharges thru a hole with diameter 2.0 mm at $\theta=225^o$ and $z=\frac{1}{4}L$.

References

[D1] "GPI Turbine Flowmeters Manufacturer specification sheet", A1 Series Commercial Grade Meter, Mobil, Accessed May 2017, https://gpimeters.com/index.php?main_page=product_info&cPath=2_4&products_id=55&zenid=61ffca7d63d6f597b00941dee531b19c

Appendix E. Effect of Sudden Flow Loss on the SFD Test Dynamic Response

SFDs stabilize aircraft engine vibration due to rotor imbalance and aerodynamic instabilities. Engine qualification requires SFDs to operate with a full loss of lubricant over a short time due to a malfunction or under a sudden 0 g maneuver load. However, actual SFD operation under this stringent condition is not known. In open ends SFDs, air ingestion causes degradation in SFDs performance due to a sudden loss of supply flow. The worst condition occurs for operation with a large whirl amplitude and a high frequency (large squeeze velocity $V_s=r\omega$).

The test rig described in the main section is used to measure the SFD response due to a sudden loss of the supply lubricant. To demonstrate a sudden loss of flow, a supply pump with a set supply pressure $P_s=3.5$ bar or 6.2 bar is shut off while the journal whirls with an orbit amplitude $r/c=0.2$ and frequency $\omega=60$ Hz.

For the PR sealed ends damper, the supply flowrate $Q_s=2.4$ LPM and 3.0 LPM for oil supply pressure $P_s=3.5$ bar and 6.2 bar; while for the O-ring sealed ends damper, $Q_s = 4.5$ LPM and 6.0 LPM for $P_s=3.5$ bar and 6.2 bar.

In the tests, the shakers excite the BC with constant frequency albeit the orbit amplitude changes. Two distinct end seals, PR and O-ring, keep the lubricant in the film land; however, the sustained whirl motion squeezes the lubricant out of the film land.

At a steady-state condition, the PR sealed ends SFD operates with a whirl amplitude $r/c=0.2$ and frequency $\omega=60$Hz. After the pump is shut off, Figures E1 and E2 show the (a) recorded journal orbit motion and (b) forces for operation with an initial supply flowrate $Q_s= 2.4$ and 3.0 LPM ($P_s=3.5$ and 6.2 bar), respectively. In the figures, lines show 1,000 recorded data (~0.6 sec, sampling rate=16,384 Hz) at every second after the pump stops. The dashed black line shows the physical limit of orbital motions, i.e., the radial clearance (c). Note the horizontal and vertical edge of the orbits show the responses are out range of the eddy current sensor.

For both initial supply pressure conditions $P_s =3.5$ and 6.2 bar, the orbit amplitude drastically increases (>300%) with time. The increase rate is larger with a larger (initial) supply flowrate $Q_s=3.0$ LPM ($P_s =6.2$ bar). On the other hand, the shaker forces decrease with time, ~20% for $Q_s=2.4$ LPM ($P_s =3.5$ bar) and ~50 % for $Q_s=3.0$ LPM ($P_s =6.2$ bar).

Interestingly, the changes in responses and forces are larger for the higher (initial) supply flowrate Q_s=3.0 LPM (P_s =6.2 bar) than those for Q_s=2.4 LPM (P_s =3.5 bar).

Similarly, for the O-ring sealed ends SFD, Figures E3 and E4 show the (a) recorded journal orbit motions and (b) shaker forces for tests with an initial supply flowrate Q_s= 4.5 LPM and 6.0 LPM (P_s=3.5 and 6.2 bar), respectively. At t=0 s (prior to flow shut down), the sealed ends SFD operates with a whirl amplitude r/c=0.2 and frequency ω=60 Hz.

Note that the BC response and force are almost identical to those for the PR sealed ends damper tests at t=0 s. Note that the orbit center immediately jumps (~0.5c) after the sudden loss of the inlet supply flow. The results are clearly distinct from the response results with the PR sealed ends SFD. Likely, the (sudden) static offset or static eccentricity is due to the interaction of the inlet and discharge holes, both having distinct static pressures.

The orbit amplitude increases (>200%) with time, whereas the forces remain constant at ~500 N. Compared with the PR sealed ends damper, the increase rate in amplitude with respect to time is lower. The amplitude response reaches a steady state value of ~150 μm and remains after 1~2 s, whereas the amplitude response for the PR sealed ends damper continuously increases.
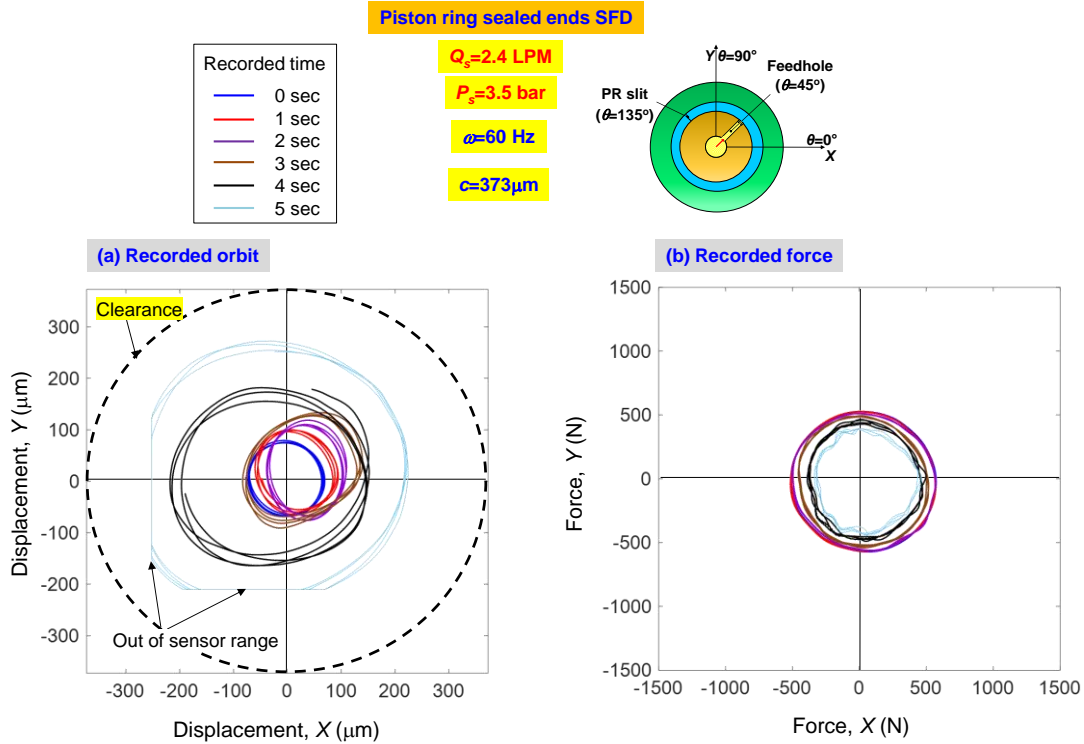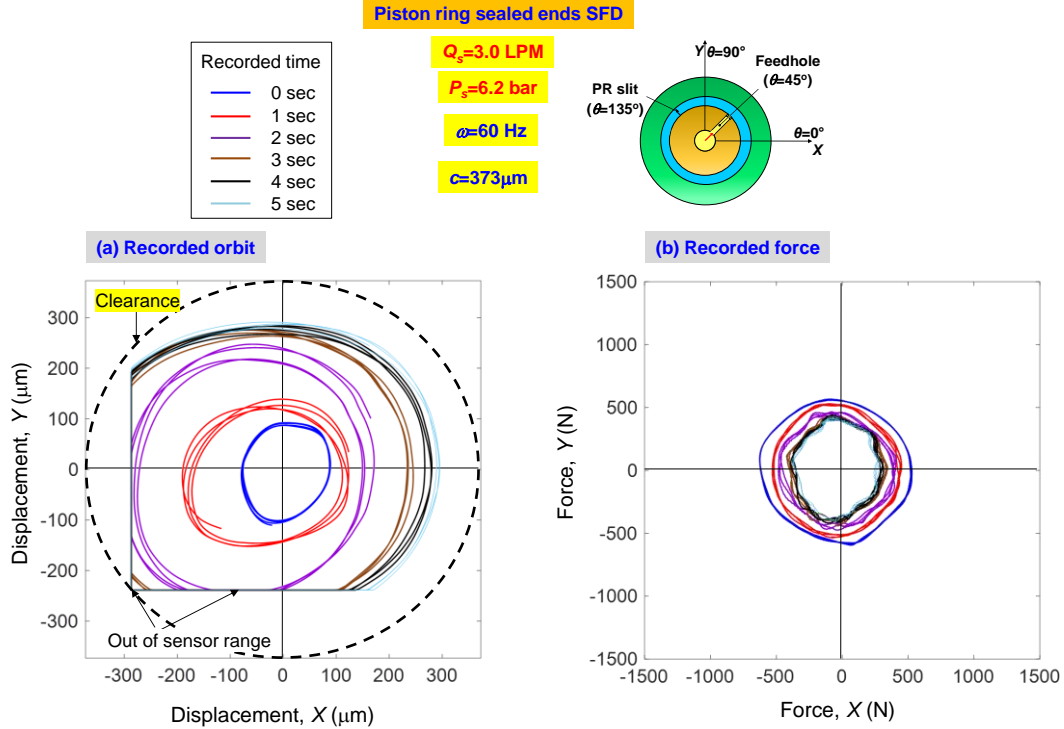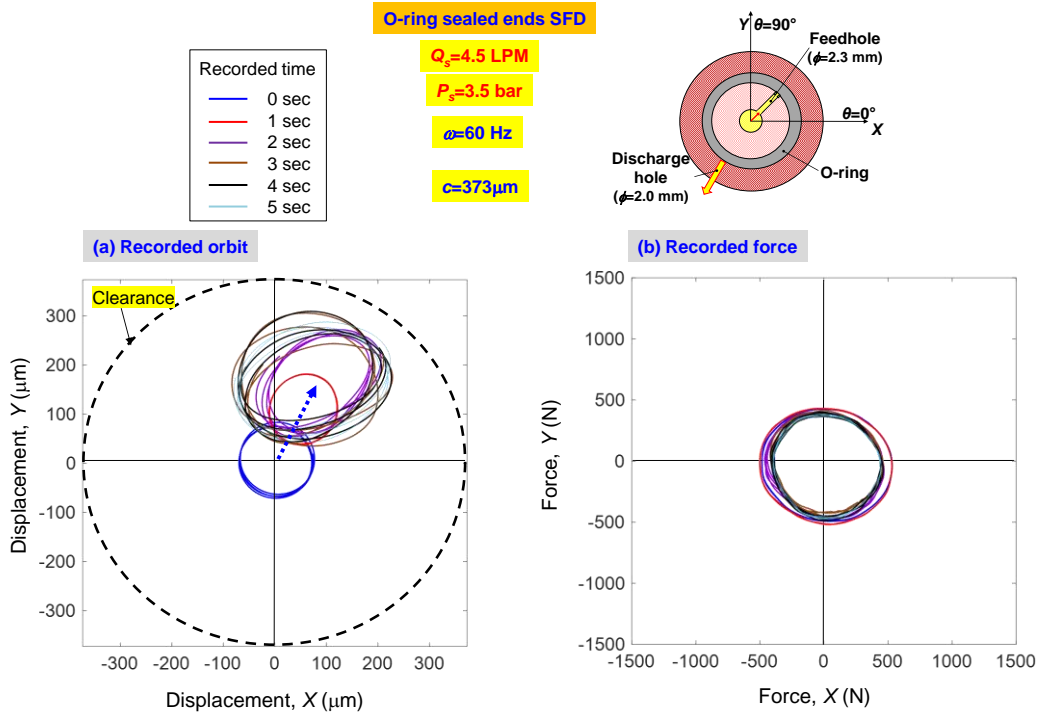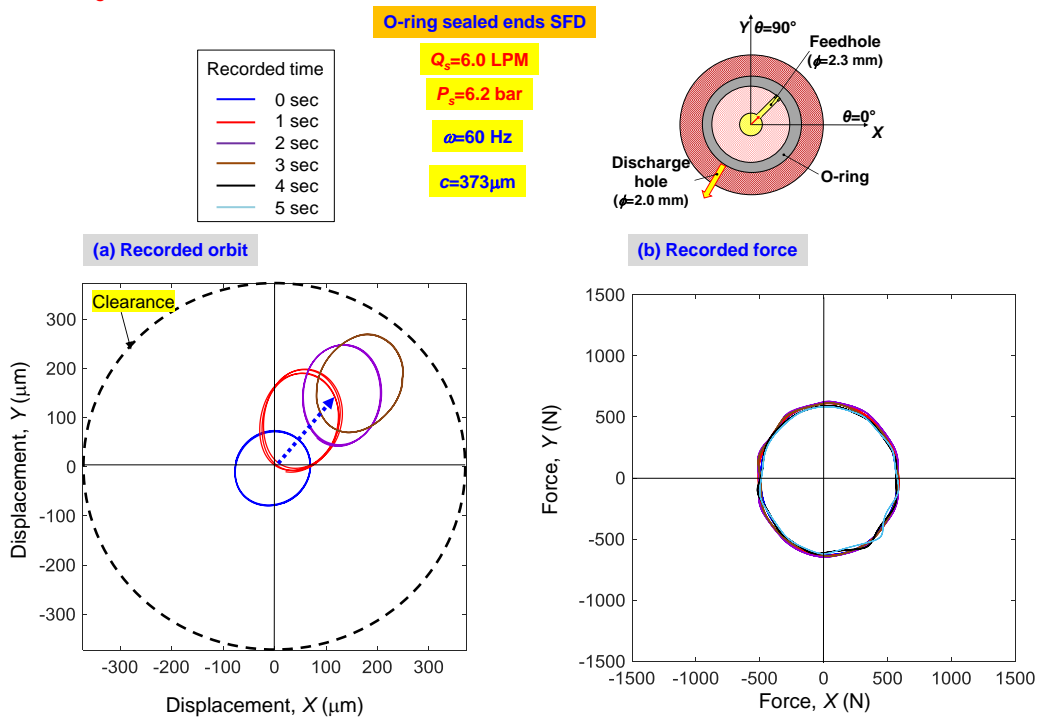
Figure E1. PR sealed ends SFD(c=373 μm): (a) Recorded journal orbit motions and (b) forces after a sudden loss of inlet supply flow. Whirl frequency ω=60 Hz. At lubricated condition (0 sec), e$_s$=0.0 r/c=0.2, Q$_s$=2.4 LPM, P$_s$=3.5 bar.

Figure E2. PR sealed ends SFD(c=373 μm): (a) Recorded journal orbit motions and (b) forces after a sudden loss of inlet supply flow. Whirl frequency ω=60 Hz. At lubricated condition (0 sec), e$_s$=0.0 r/c=0.2, Q$_s$=3.0 LPM, P$_s$=6.2 bar.

Figure E3. **O-ring sealed ends SFD(c=373 μm):** **(a) Recorded journal orbit motions and (b) forces after a sudden loss of inlet supply flow. Whirl frequency ω=60 Hz. At lubricated condition (0 sec), e_s=0.0 r/c=0.2, Q_s=4.5 LPM, P_s=3.5 bar.**

Figure E4. **O-ring sealed ends SFD(c=373 μm):** **(a) Recorded journal orbit motions and (b) forces after a sudden loss of inlet supply flow. Whirl frequency ω=60 Hz. At lubricated condition (0 sec), e_s=0.0 r/c=0.2, Q_s=6.0 LPM, P_s=6.2 bar.**

Figures E5-E8 show waterfall plots of the recorded BC displacements (x, y) and forces during ~8 s after the sudden loss of the supply flow. The data are reproduced from the results shown in Figs. E1-E4. The waterfall plots show a dominant frequency at ω=60 Hz albeit the PR sealed ends damper has a small (~10%) 2X frequency (120 Hz) component and a DC offset.

Again, the waterfall plots show that the amplitude responses increase with time after the supply flow is shut off, whereas the applied force decreases. After a few seconds, the response amplitude (x, y) increase to thrice and twice the response at t=0 s for the PR and O-ring sealed ends SFDs, respectively. Note the response for the PR sealed ends damper exceeds the sensor range; thus the actual response is probably larger than the recorded magnitude. For the O-ring sealed ends SFD, the response suddenly jumps with a sudden loss of the supply flow.

In brief, with a complete loss of a lubricant, the sealed ends SFD amplitude of dynamic response quickly increases. The effect of the lubricant loss on the SFD response is more significant when the initial supply flow (Q_s) [pressure (P_s)] is large. After the flow is cut, and as the transient response ensues, the O-ring sealed ends damper shows a smaller amplitude of motion than that for the PR sealed ends damper. Likely, the O-ring stiffness and damping come into place to limit the motion.
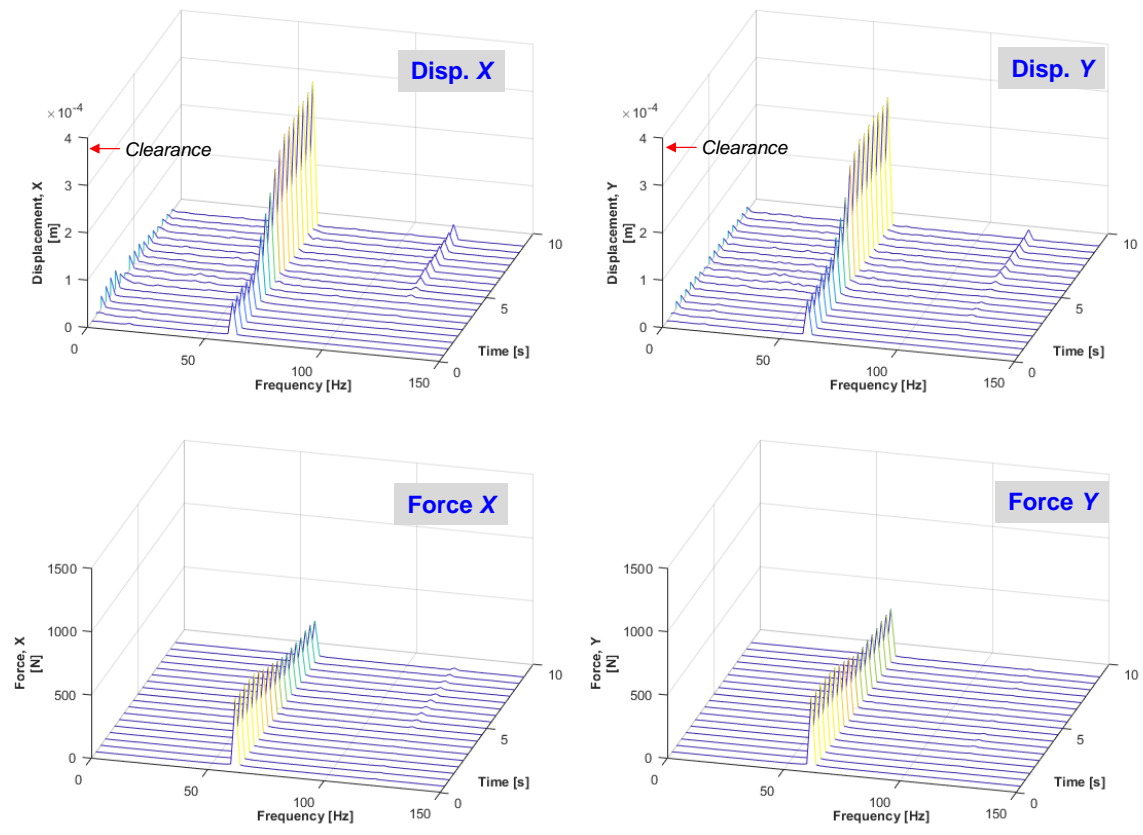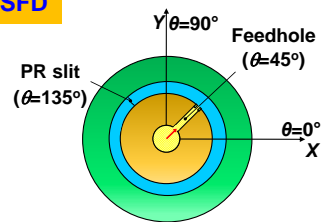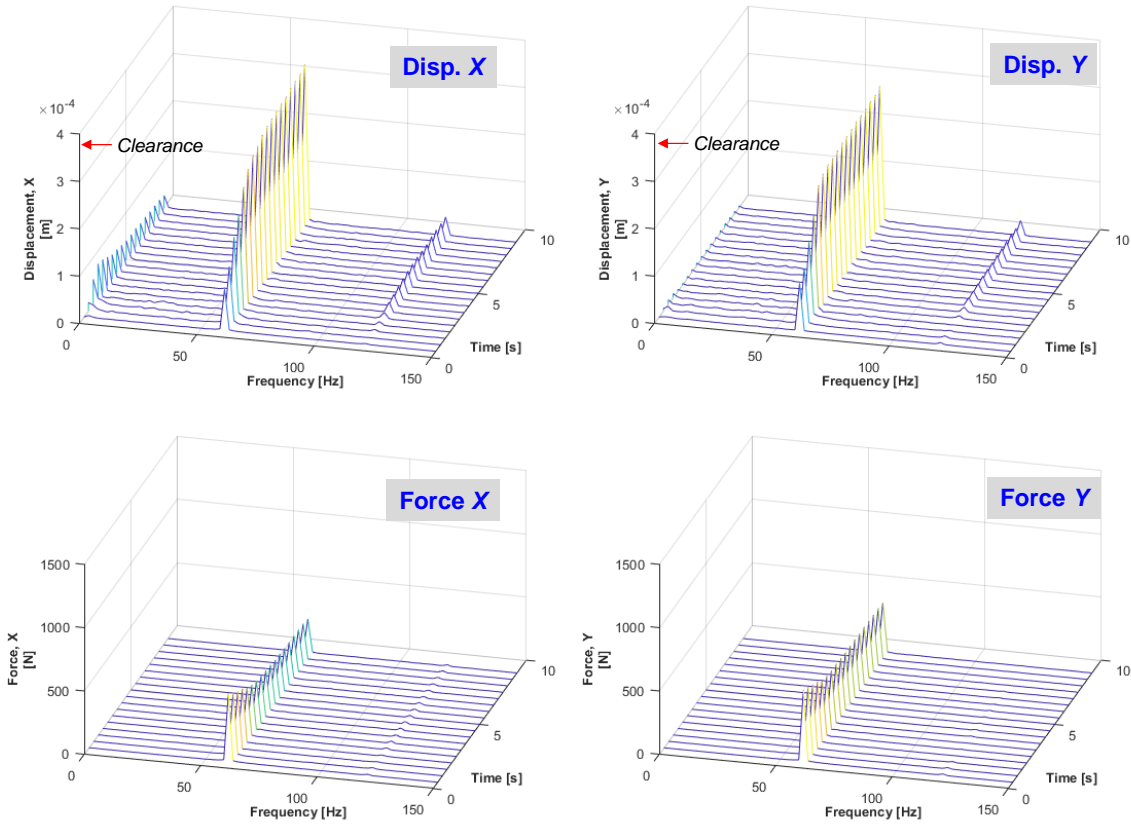
Figure E5. PR sealed ends SFD(c=373 μm): Waterfall of (a) recorded journal orbit motions and (b) forces (X, Y) during 8 secs after a sudden loss of inlet supply flow. Whirl frequency ω=60 Hz. At lubricated condition (0 sec), e_s=0.0, r/c=0.2, Q_s=2.4 LPM, P_s=3.5 bar.
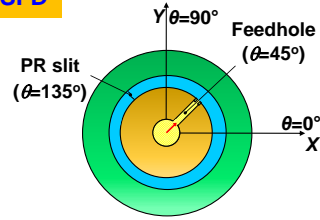
Figure E6. PR sealed ends SFD(c=373 μm): Waterfall of (a) recorded journal orbit motions and (b) forces (X,Y) during 8 secs after a sudden loss of inlet supply flow. Whirl frequency ω=60 Hz. At lubricated condition (0 sec), e_s=0.0, r/c=0.2, Q_s=3.0 LPM, P_s=6.2 bar.
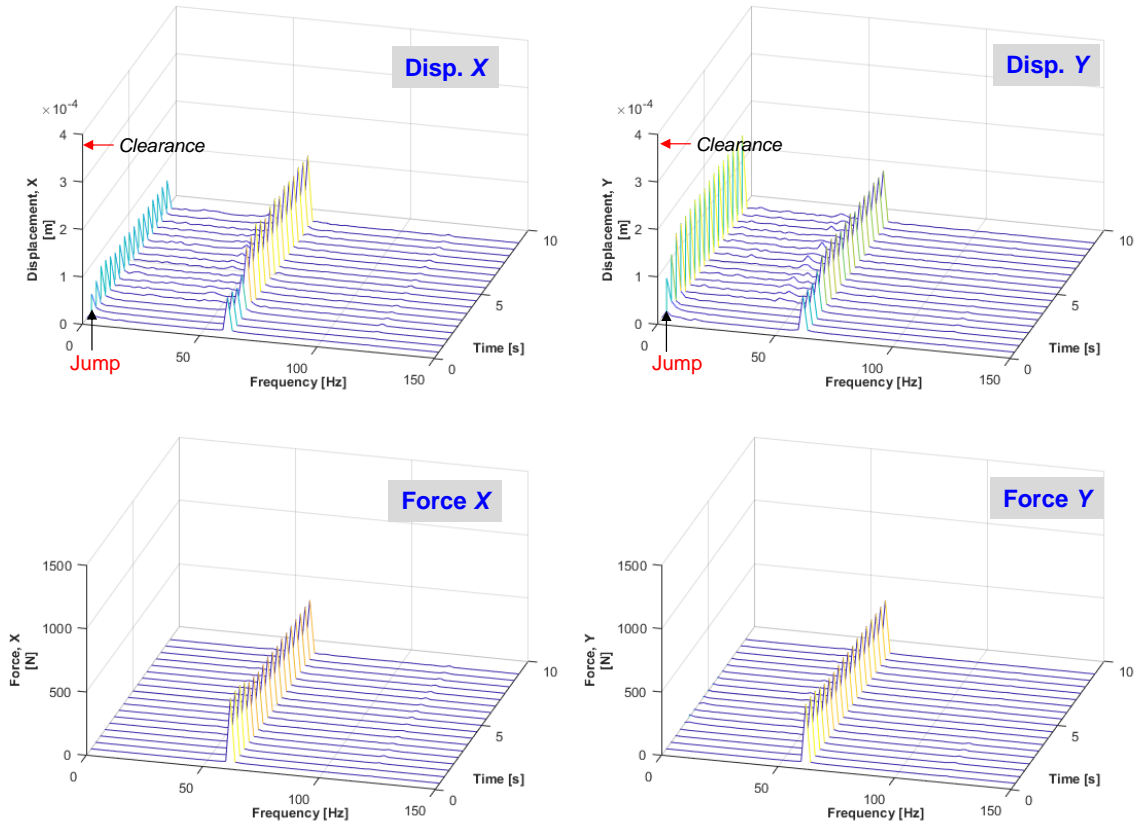
Figure E7. O-ring sealed ends SFD(c=373 μm): Waterfall of (a) recorded journal orbit motions and (b) forces (X, Y) during 8 secs after a sudden loss of inlet supply flow. Whirl frequency ω=60 Hz. At lubricated condition (0 sec), e$_s$=0.0, r/c=0.2, Q$_s$=4.5 LPM, P$_s$=3.5 bar.
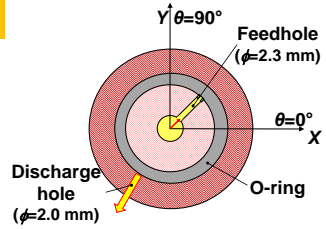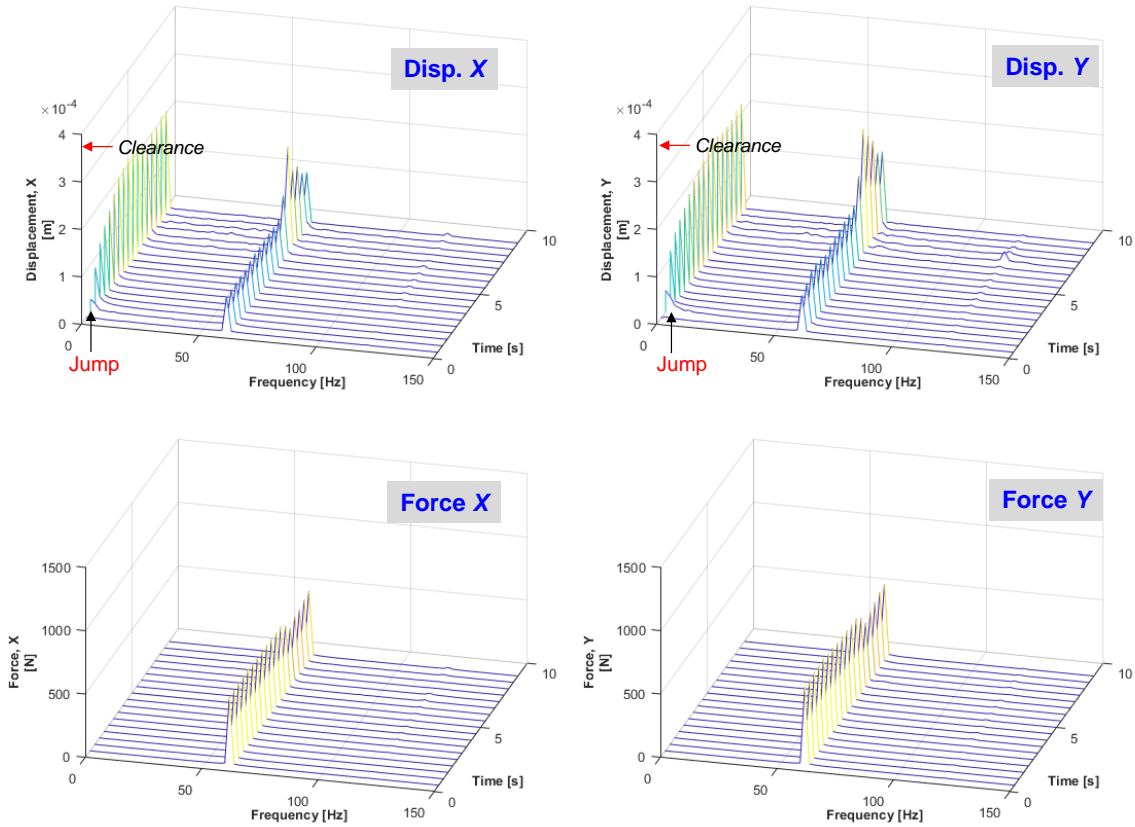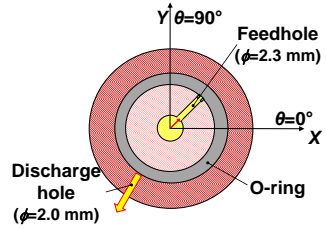
Figure E8. O-ring sealed ends SFD(c=373 μm): Waterfall of (a) recorded journal orbit motions and (b) forces (*X*, *Y*) during 8 secs after a sudden loss of inlet supply flow. Whirl frequency ω=60 Hz. At lubricated condition (0 sec), e_s=0.0, r/c=0.2, Q_s=6.0 LPM, P_s=6.2 bar.

Appendix F. SFD Cross-coupled Dynamic Stiffnesses

For the PR sealed ends and O-ring sealed ends SFDs, Figures F1 and F2 show the real and imaginary parts of the cross coupled dynamic stiffness $\text{Re}(H_{XY}, H_{YX})_L$, $\text{Im}(H_{XY}, H_{YX})_L$, respectively, as well as the physical curve fits (KCM model). For P_s=0.7 bar and 6.2 bar, the SFDs operates with the whirl radius r/c=0.3. The inset tables list the cross-coupled damping and mass coefficients as well as the curve fit correlation factors to the KCM model. From the low values of the correlation factors $R^2 < 1$, it is evident that the model parameter does not reproduce the measured complex dynamic stiffness (H_{XY}, H_{YX}). Furthermore, compared with the direct complex stiffnesses (H_{XX}, H_{YY}) in Figs. 5 and 6, the slopes are much smaller; i.e., $(C, M)_{XY,YX}$ are at least one order of magnitude smaller. .
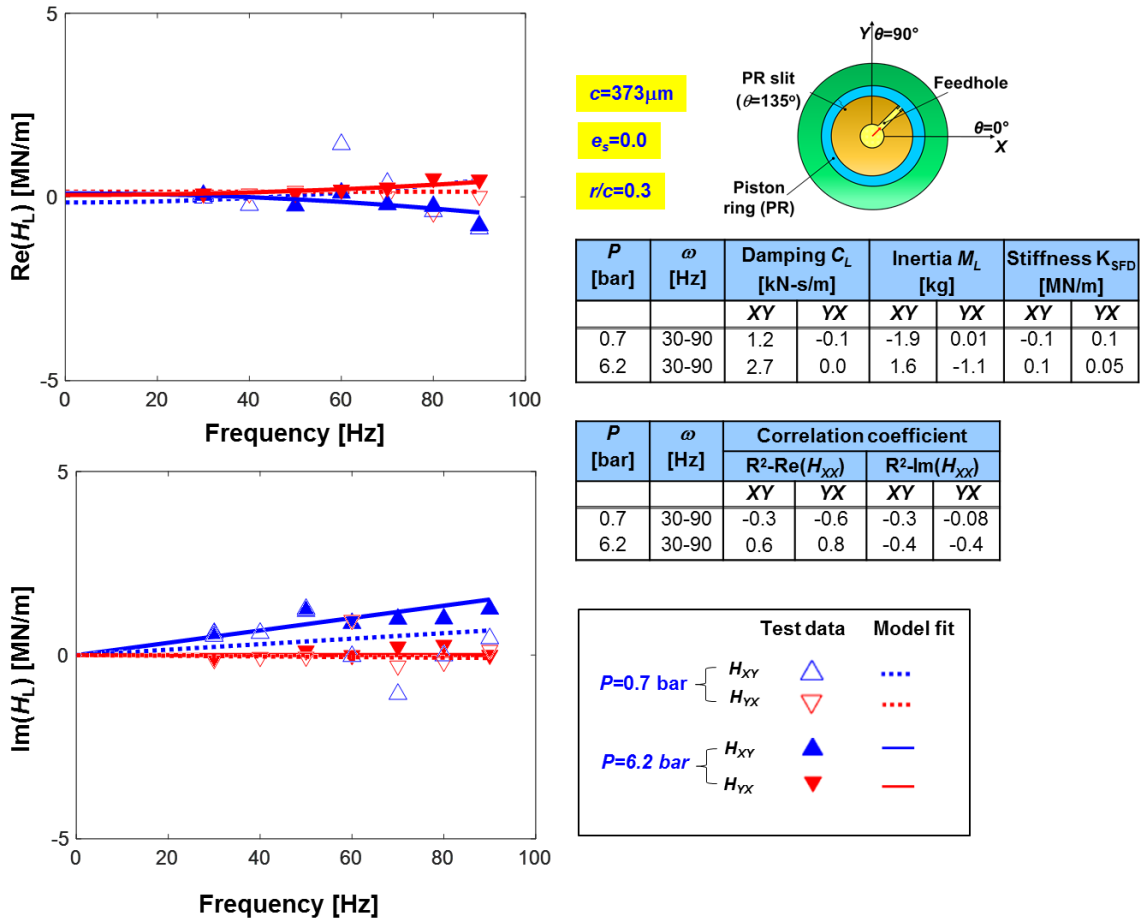
Figure F1. PR sealed ends damper (c=373 μm): Real and imaginary parts of cross couple complex stiffness for lubricated system $(H_{XY}, H_{YX})_L$ vs. whirl frequency. Circular centered orbits with radius r/c=0.3 (e_s=0). Whirl frequency range ω=30-90 Hz. Lubricant supplies thru a feedhole at θ=45° with supply pressure P_s=0.7 and 6.2 bar. PR slits locate at θ=135°.

The charts contain the following annotated values:

c=373μm
e_s=0.0
r/c=0.3

P [bar]	ω [Hz]	Damping C_L [kN-s/m]		Inertia M_L [kg]		Stiffness K_{SFD} [MN/m]	
		XY	YX	XY	YX	XY	YX
0.7	30-90	-2.9	0.7	-3.8	0.4	-0.43	0.21
6.2	30-90	0.4	0.2	-2.5	-1.4	-0.32	-0.32

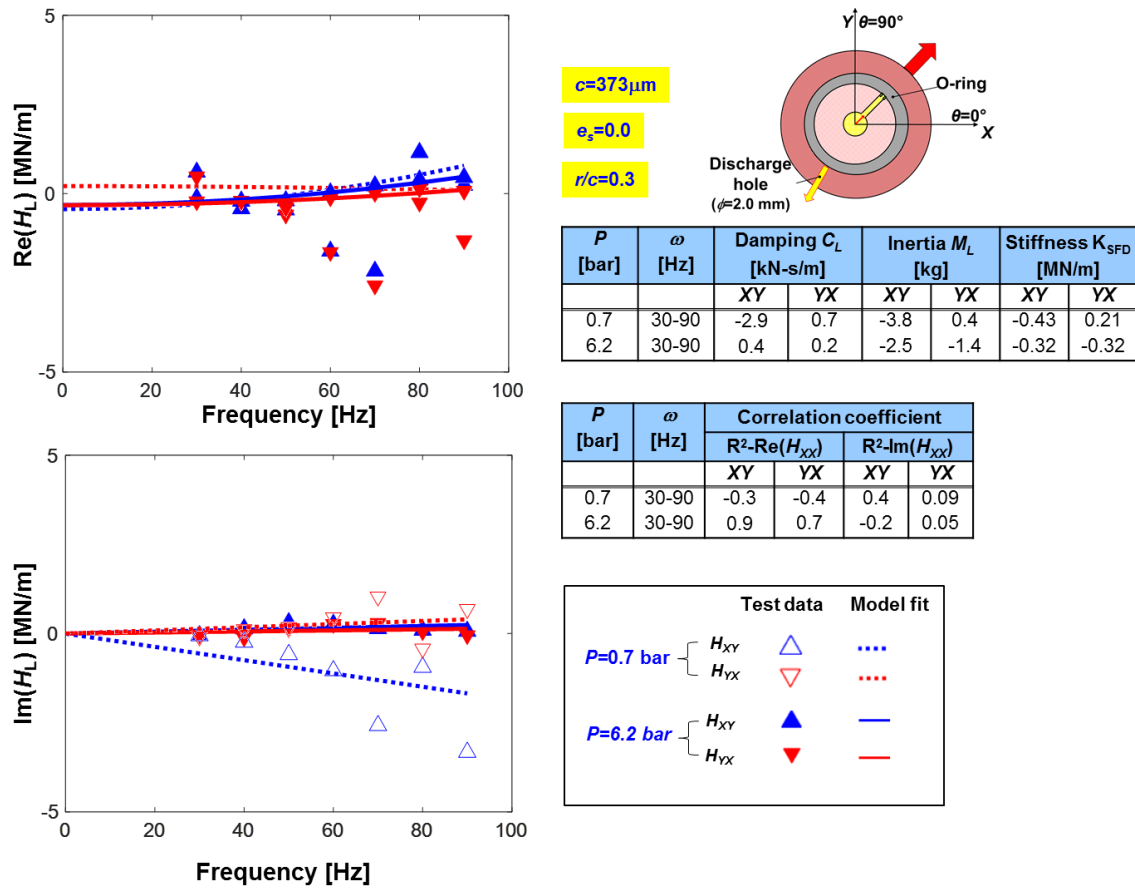| P [bar]	ω [Hz]	Correlation coefficient			
		R^2-Re(H_{XX})		R^2-Im(H_{XX})	
		XY	YX	XY	YX
0.7	30-90	-0.3	-0.4	0.4	0.09
6.2	30-90	0.9	0.7	-0.2	0.05

Figure F2. O-ring sealed ends damper (c=373 μm): Real and imaginary parts of cross-couple complex stiffness for lubricated system (H_{XY}, H_{YX})$_L$ vs. whirl frequency. Circular centered orbits with radius r/c=0.3 (e_s=0). Whirl frequency range ω=30-90 Hz. The lubricant supplies thru a feedhole at θ=45° with lubricant supply pressure P_s=0.7 and 6.2 bar. A discharge hole locates at z=¼ L and θ=225°.

Appendix G. Complex Dynamic Stiffness Measurements: PR Sealed Ends SFD with Small Orbit Radius (r/c=0.1)

For the PR sealed ends damper describing orbits with radius r/c=0.1, Figure G1 shows Re(H_{XX}, H_{YY})$_L$, Im(H_{XX}, H_{YY})$_L$, as well as the physical curve fits (KCM model). The lubricant supply pressure ranges from 2.1 to 6.2 bar. The inset table shows the SFD direct force coefficients ($\mathbf{H}_{SFD}=\mathbf{H}_L-\mathbf{H}_S$) and the curve fit correlation factors validating the KCM model. Since Ima(H) shows a large amplitude intercept (H_0) along the vertical axis (ω=0), the appropriate model for identification is Im(H)=$H_0+\omega C$, as shown by the lines in the bottom graph. For this model, $R^2 \sim 1$.

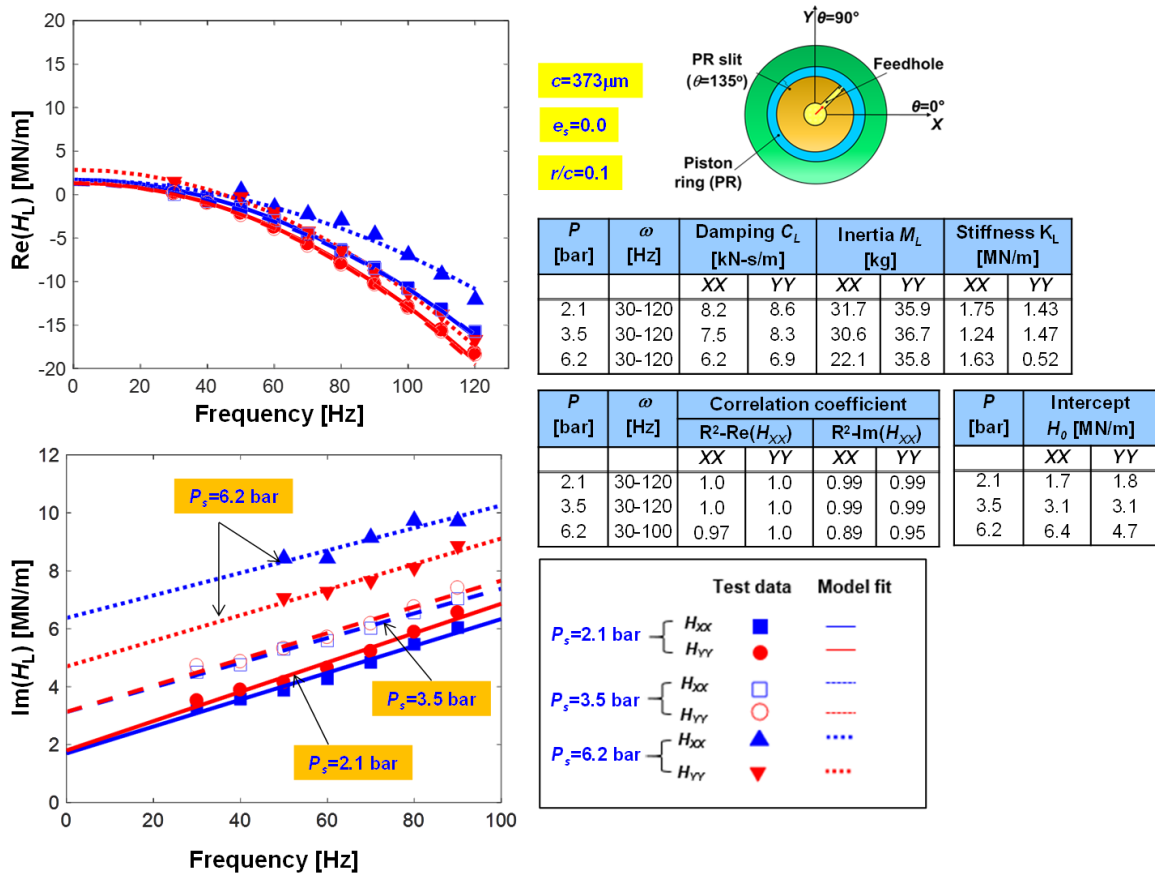| P [bar]	ω [Hz]	Damping C_L [kN-s/m]		Inertia M_L [kg]		Stiffness K_L [MN/m]	
		XX	YY	XX	YY	XX	YY
2.1	30-120	8.2	8.6	31.7	35.9	1.75	1.43
3.5	30-120	7.5	8.3	30.6	36.7	1.24	1.47
6.2	30-120	6.2	6.9	22.1	35.8	1.63	0.52

P [bar]	ω [Hz]	Correlation coefficient				P [bar]	Intercept H_0 [MN/m]	
		R^2-Re(H_{XX})		R^2-Im(H_{XX})				
		XX	YY	XX	YY		XX	YY
2.1	30-120	1.0	1.0	0.99	0.99	2.1	1.7	1.8
3.5	30-120	1.0	1.0	0.99	0.99	3.5	3.1	3.1
6.2	30-100	0.97	1.0	0.89	0.95	6.2	6.4	4.7

Figure G1. PR sealed ends damper (c=373 μm): Real and imaginary parts of direct complex stiffness for lubricated system (H_{XX}, H_{YY})$_L$ vs. whirl frequency. Circular centered orbits with radius r/c=0.1 (e_s=0). Whirl frequency range ω=10-120 Hz. Lubricant flows thru a feedhole at θ=45° with supply pressure P_s=1.4, 3.5, and 6.2 bar. PR slits locate at θ=135°

Note the identified M is similar to that for orbits with r=0.3c (see Fig. 6). On the other hand, the damping C appears to decrease with an increase in lubricant supply

pressure. Note, however, that H_0 grows as the supply pressure rises. The appearance of H_0 is due to a sliding friction or stick-slip effect between the PR seals and the groove surfaces. Figure G2 shows a worn surface of the PRs evidencing the relative motion between the PRs within its journal grooves.
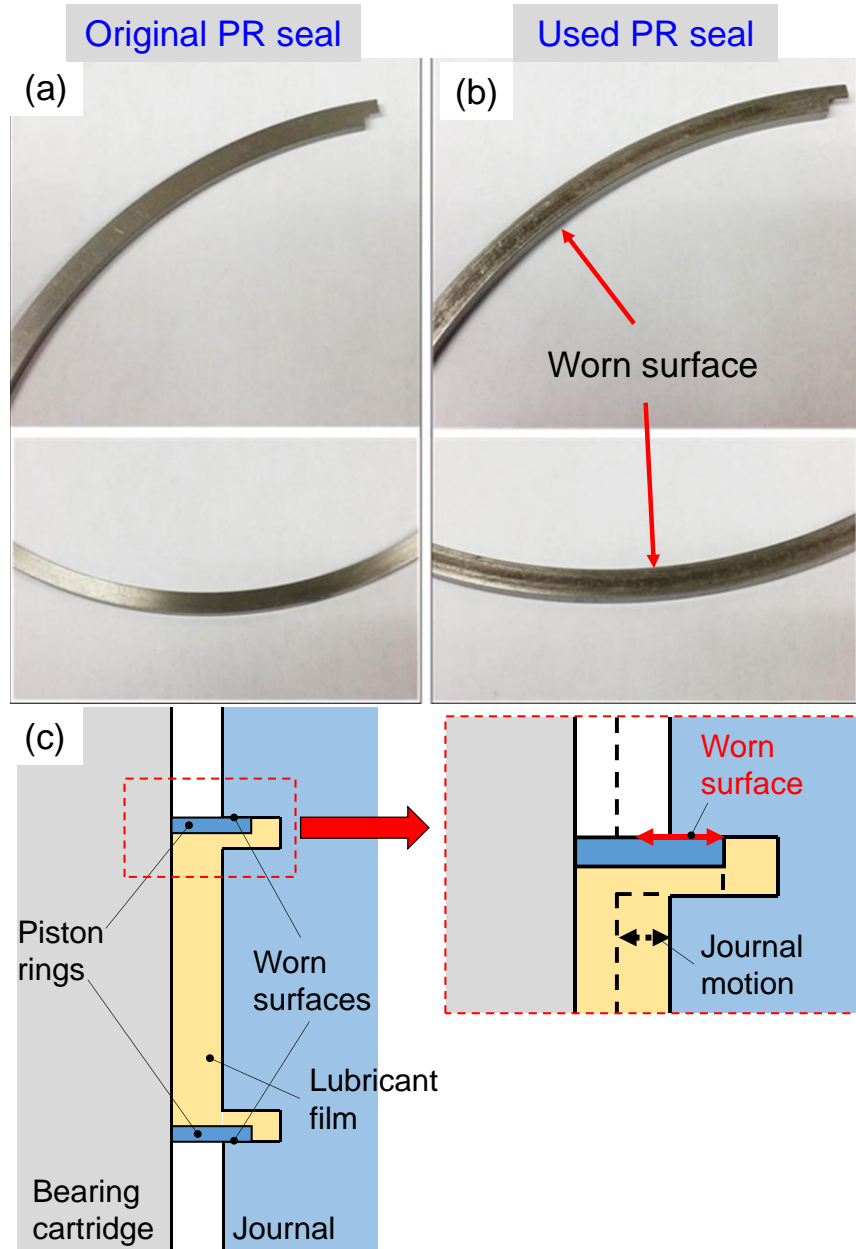

Figure G2. Photographs of (a) original piston ring (PR), (b) used PR with worn marks after dynamic load tests. (c) Schematic view shows locations of worn surfaces with PRs installed.